Phosphate Petrochronology of the Belcina REE Mineralization (Ditrău Alkaline Massif, Romania)

Urs Klötzli *, Jolanta Burda , Paul Tibuleac

Posted Date: 5 May 2023

doi: 10.20944/preprints202305.0299.v1

Keywords: Phosphate petrochronology; Ditrău Alkaline Massif; Eastern Carpathians; REE mineralization; Metasomatism; Hydrothermal fluids

Article

Phosphate Petrochronology of the Belcina REE Mineralization (Ditrău Alkaline Massif, Romania)

Urs Klötzli [1,*], Jolanta Burda [2] and Paul Tibuleac [3]

[1] Department of Lithospheric Research, University of Vienna, Josef-Holaubek-Platz 2, 1090 Vienna, Austria; urs.kloetzli@univie.ac.at

[2] Institute of Earth Sciences, Faculty of Natural Sciences, University of Silesia in Katowice, 41-200 Sosnowiec, Poland; jolanta.burda@us.edu.pl

[3] Department of Geology, University Alexandru Ioan Cuza of Iasi, Boulevard Carol I, 20 A, 700506 Iasi, Romania; paul.tibuleac@uaic.ro

* Correspondence: urs.kloetzli@univie.ac.at; Tel.: 0043-1-4277-53460

Abstract: A notable REE mineralization in Europe is associated with the Ditrău Alkaline Massif (DAM) in the Eastern Carpathians (Romania). It is an expression of the latest hydrothermal phase in the DAM and is found in the form of mineralized carbonate veins cross-cutting the complex in the NW (Jolotca region) and the SE (Belcina region) parts of the DAM. In the Belcina veins monazite-(Ce), xenotime-(Y), apatite, together with Fe-Mg-rich carbonate, thorite, thorogummite, gedrite and plagioclase are rock-forming. Three different textural and chemical types of the monazite-(Ce) and the xenotime-(Y) document a three-stage evolution. The relative phosphate age succession (from older to younger) thereby is xnt1 > xnt2 (>)+ mnz1 + Fe2O3 + Fe-gedrite > mnz2 + Fe-dolomite (+ plagioclase) > mnz3 + xnt3 + apatite. Phosphate chemistry shows that these crystallized from hydrothermal fluids, whereby each phosphate type follows a separate evolutionary path recommending growth from (at least) 3 independent and successive hydrothermal fluids. Chemistry and pathways within the DAM suggest that these hydrothermal fluids could be derived from a subsurface carbonatitic intrusion. Mnz1,2 and xnt1,2 ages are tightly cluster at 215.8 ± 0.7 Ma (Norian, Upper Triassic). The third-generation phosphate ages are younger, but associated with large analytical uncertainties and did not deliver geologically useful ages. The mean age of ca. 216 Ma is interpreted as timing the Belcina REE mineralization, what together with the fluid chemistry, supports a model of the presence of a late-stage, independent carbonatitic intrusion about 10 Ma after the main igneous activity (ca. 235 - 225 Ma) forming the DAM, synchronous with extension-related magmatism in the region.

Keywords: Phosphate petrochronology; Ditrău Alkaline Massif; Eastern Carpathians; REE mineralization; Metasomatism; Hydrothermal fluids

1. Introduction

Alkaline rocks are a minor but important component of the continental crust. They usually contain significant amounts of rare metals such as Li, Be, Nb, Ta, Zr, Th, REE and volatile components, mainly F and Cl. One of the most notable REE mineralization in Europe, having significant economic importance, is associated with the ca. 235-225 Ma Ditrău Alkaline Massif DAM) in the Eastern Carpathians of Romania (Figure 1, [1,2]). REE-rich mineral veins are found within the alkaline complex at Jolotca, and outside the complex at Belcina regions (Figure 2).

The Belcina carbonate vein REE mineralization is localized in the ESE of the DAM within the metamorphic Cambrian Putna Nappe (Figure 2; e.g. [3–6]. The first mineralogical description of the Belcina carbonate vein REE mineralization was given by [7] that was subsequently complemented by [8], and references therein). A thorite ($(Th,U)SiO_4$), thorogummite ($(Th,U)(SiO_4)_{1-x}(OH)_{4x}$), xenotime-(Y) ($YPO_4$) paragenesis represent the characteristic mineral association of the Belcina mineralization. Other common minerals are monazite-(Ce) and Th-rich apatite, zircon, Nb-rutile, ferrocolumbite, Y-

Preprints (www.preprints.org) | NOT PEER-REVIEWED | Posted: 5 May 2023 doi:10.20944/preprints202305.0299.v1

fluorite, and minor amounts of Nb-Ta-pyrochlores, brabantite, allanite, REE(Y)-carbonates (e.g. bastnaesite), Fe-oxides and hydroxides (magnetite, hematite, goethite, lepidocrocite), sulphides (pyrite, arsenopyrite, galena, sphalerite, chalcopyrite, tetrahedrite, molybdenite, cinnabar) and native mercury. The gangue associated with the ore is formed by feldspars (microcline, albite, orthoclase), quartz, different carbonates of at least two generations (calcite, ferrodolomite, siderite), natrolite, pectolite and chlorites [8]. According to [9] the mineral succession found in the Belcina mineralization is apatite > xenotime-(Y) > thorite. According to [4,6] the Belcina mineralization is genetically linked to the Lăzarea suite. But [5] stated that the fluid responsible for the mineralization is connected to the late-stage hydrothermal overprinting event. Preliminary mineral data suggest that xenotime-(Y) has a constant and relatively pure composition, with of about Y_2O_3 ~ 60 - 62 weight-% and P_2O_5 ~ 38 - 40 weight-% [8]. On the other hand, [9] reports that the xenotime-(Y) is rich in HREE with up to 6 weight-% Dy, 5 weight-% Yb, 4 weight-% Gd and Er. A more detailed mineralogical description of the Belcina veins is given in [8,9].

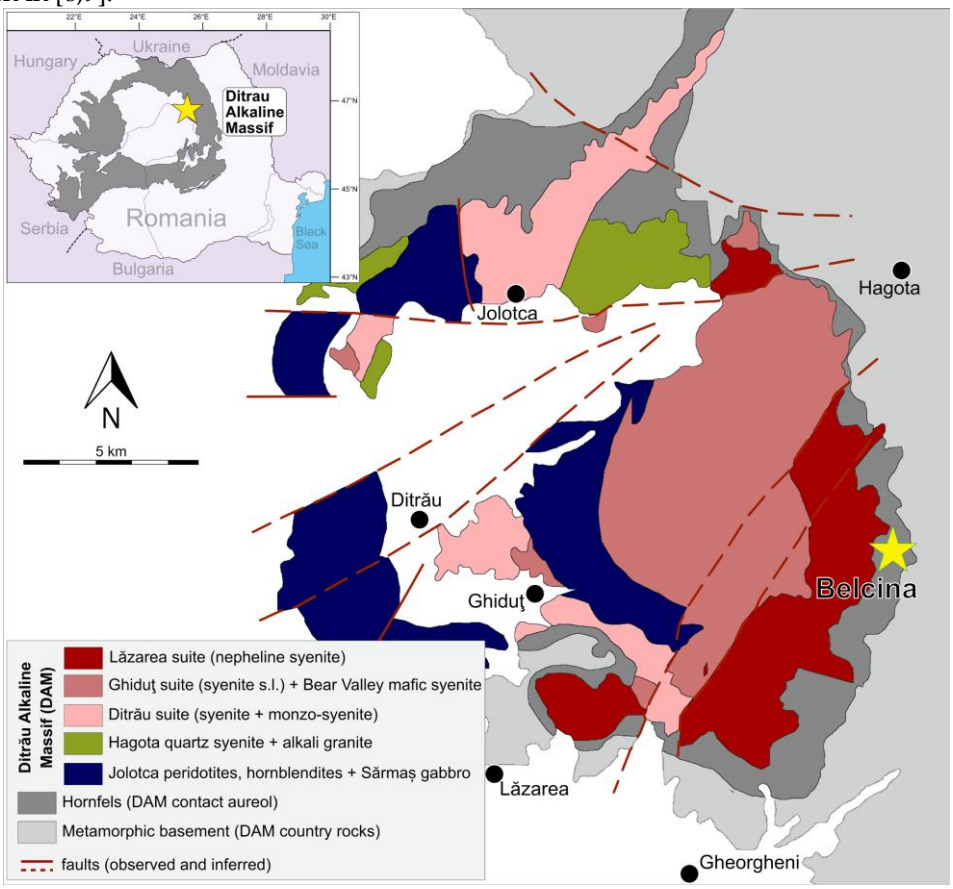

Figure 1. Geological sketch map of the Ditrău Alkaline Massiv modified after [2,5]. The location of the Belcina sample is indicated by the yellow star. The inset shows the position of the Ditrău Alkaline Massiv within the Eastern Carpathians.

Preprints (www.preprints.org) | NOT PEER-REVIEWED | Posted: 5 May 2023 doi:10.20944/preprints202305.0299.v1

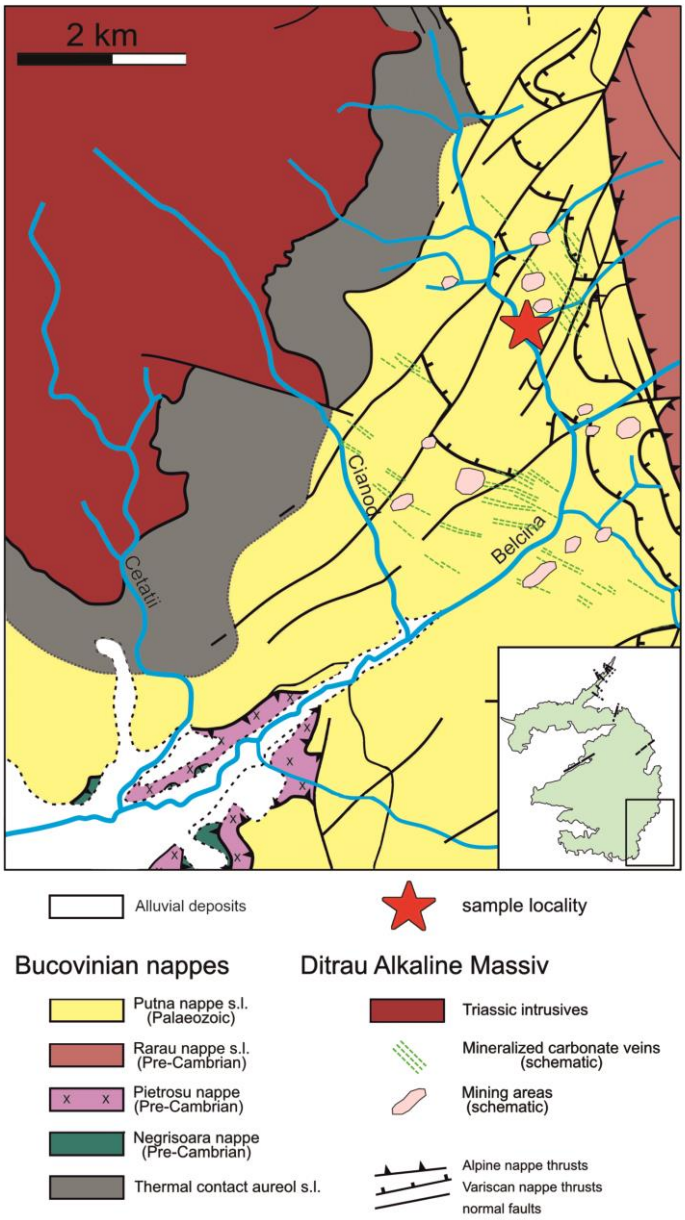

Figure 2. Detailed geological sketch map of the SE part of the Ditrău Alkaline Massiv modified after [5,6]. The location of the investigated carbonate mineralized vein sample in the Belcina valley is indicated by the red star.

The total concentration of REE in average bulk continental crust is ca. 125 ppm [10]. Enrichment of the REE may occur through primary processes such as magmatic processes and hydrothermal fluid mobilization and precipitation, or through secondary processes (e.g., [11]). What remains to be understood are the specific relations between the degree of mineralization and the underlying processes, the petrology and the age systematics of such rock suites. Monazite-(Ce) and xenotime-(Y) belong to the most important carriers of REEs. A detailed study of their composition, stability and breakdown processes provides us with an understanding of REE relationships and processes that occur during petrogenesis and evolution of the parental rock [12–19] and references therein). Although numerous geochronological studies have been published from the DAM (for reviews see [1,2]), no dating of the Jolotca and Belcina REE mineralizations have yet been undertaken.

Here we report the mineral chemistry and the growth-age systematics of monazite-(Ce) and xenotime-(Y) from a late-stage REE mineralized carbonate vein situated in the contact aureole of the DAM in the Belcina region of the DAM. We show that the vein formation follows a distinctive three-

 doi:10.20944/preprints202305.0299.v1

stage evolutionary pattern and is around 10 My younger (at ca. 216 Ma) than the youngest known igneous activity of the DAM (at ca. 225 Ma). We then integrate and discuss these data into existing evolutionary models of the DAM [1,2,5,20].

2. Geological Background

Overview

The Ditrău Alkaline Massif (DAM) is an alkaline igneous massif in the Eastern Carpathian Mountains in Romania (Figure 1). It has the potential to contribute to a secure and sustainable European REE mining industry, ensuring supply security for these critical metals [5], and therefore being of major geological interest.

It was emplaced in an extensional, rift-related continental intraplate setting related to the opening of the Meliata-Hallstatt Ocean in the Middle to Upper Triassic [21]. The country rocks of the DAM are pre-Middle Triassic metamorphic rocks of the Alpine Bucovinian Nappe (e.g. [22]). The complex is partially covered by Neogene volcanics and Pliocene-Pleistocene lacustrine sediments [6,5]. The detailed petrography and petrology of the DAM rocks have formerly been described by (e.g. [2,5,20] and references therein).

The following main lithologies can be distinguished (Figure 1): In the western and northern part of the DAM mafic–ultramafic cumulate rocks ranging from peridotites, pyroxenites, and hornblendites (*Jolotca hornblendites* [5,23]) to alkali gabbros (*Sărmaș gabbro* [5]) and alkali diorites (*Bear-valley mafic syenite* [24]) occur. Quartz syenites and alkali granites are found in the Jolotca area and the north-eastern DAM (*Hagota quartz syenite* [5]). East of a line Jolotca - Ditrău - Lăzarea - Gheorgheni the DAM is dominated by alkaline intrusive suites. Based on geochemical and geochronological data three magmatic suites can be distinguished [2]:

- Ditrău suite, comprising syenites to monzo-syenites (equivalent to the *'Ditrău syenite*' of [5] and dated at 230.7 ± 0.2 Ma;

- Ghiduţ suite, comprising nepheline syenites, subordinate syenites, and monzo-syenites (equivalent to the former *ditroite* and the *white nepheline syenite* [6,24,25] and the 'Ghiduţ nepheline syenite' [5] dated at 231.1 ± 0.8 Ma;

- Lăzarea suite, comprising weakly to very strongly altered nepheline syenites (formerly *red syenite* [7] or *red, hydrothermally altered variety* [24]) dated at 224.9 ± 1.1 Ma.

The DAM is surrounded by a thermal contact aureole (labeled as 'Hornfelses' on Figure 1) which developed in the low-grade metasedimentary country rocks [28].

All lithological units have been significantly modified by near-solidus to sub-solidus interaction with late-stage magmatic fluids and were cut by secondary mafic dykes [20,26,27]. The hydrothermal system is believed to have developed within the DAM magma chamber during the later stages of magmatic crystallization [5,25], causing the localized alteration of nepheline syenites by a Na-rich fluid. In addition, mafic dykes allowed the upward migration of late-stage K-rich fluids, thereby leaching REE and HFSE from the Ghiduţ suite [5,20]. The DAM and country rocks were subsequently also invaded by carbonate- and REE-enriched fluids forming veins in which rock-forming monazite-(Ce) and xenotime-(Y) crystallized among a complex suite of other minerals. These veins mostly crosscut the complex in the north-western (Jolotca region) and the south-eastern (Belcina region) parts of the DAM [3-5].

A number of genetic models have been published, but no consensus as to the evolution of the DAM has been reached so far (see [2] and references therein).

3. Analytical Methods

3.1. Optical Microscopy

The petrography and thin section imaging was carried out using a NIKON petrographic microscope and a Keyence VHX-5000 digital microscope at the Department of Lithospheric Research, University of Vienna, Austria.

 doi:10.20944/preprints202305.0299.v1

3.2. Backscattered Electron Imaging

The textures and chemical zonations of the Belcina phosphates were revealed by backscattered electron imaging using a FET Philips 30 electron microscope, an accelerating voltage of 15 kV and a beam current of 20 nA at the Institute of Earth Sciences, University of Silesia in Katowice, Poland. The most suitable location of the spots for the EMP mineral analyses and (U+Th)-Pb dating were selected based on these images.

3.3. EMP Mineral Analyses

Mineral chemistry analyses of monazite-(Ce) and xenotime-(Y) were performed using a Cameca SX 100 electron microprobe equipped with five wavelength dispersive spectrometers (WDS) at the Micro-area Analyses Laboratory of the Polish Geological Institute (Warsaw, Poland), using 15keV acceleration voltage, 40nA beam current, 1 μm beam width. The counting times for peaks were set to 30-60 seconds for REEs and As, 20 seconds for others. The counting times for the background positions were a half time for each peak; Pb Mβ, Th Mα, U Mβ were determined using 15keV, 300nA, 1 μm, counting time for peaks for monazite-(Ce) analysis: 60 seconds for Th, 160 seconds for U and 240 seconds for Pb and for xenotime-(Y) analysis: 200 seconds for Th, 160 seconds for U and 300 seconds for Pb. Counting time for measured U, Th and Pb background was the same as for each peak, wherein two background positions were measured for each element. Calibration was conducted on natural and synthetic standards: REEs and Y were obtained from synthetic orthophosphates [XPO_4], Th and U from synthetic glasses enriched with Th and U, Pb from pyromorphite, Fe from hematite, Zr from synthetic ZrO_2, P from apatite, As from arsenopyrite, S and Sr from synthetic celestite [$SrSO_4$], Ca and Si from wollastonite, K and Al from orthoclase.

Peak overlaps were deconvoluted following the method described by [29]: U Mb corrected for Th Mγ, K Kα; Lu Lβ corrected for Ho Lγ, Yb Lβ2; Tm Lβ, corrected for Tn Lγ, Gd Lγ2; As Lβ, corrected for Dy Mβ; Hf Lα, corrected for Er Mγ; Zr Lα, corrected for P Kα. No correction for overlapping Zr Lα by P Kα was made because both peaks were measured on PET crystals, where peaks are well separated. The reported concentration values are either given as weight-% or μg/g.

3.4. EMP U+Th- Total Pb Dating

U+Th-total Pb spot ages were calculated using the mathematical expressions of [30,31]. A 2-standard deviation uncertainty on the apparent age was estimated from each single spot analysis by propagating the 1-standard deviation absolute weight-% uncertainty of the Pb, Th, and U abundances, respectively, as computed by the Cameca SX100 software, through the U+Th-total Pb age equation. The CHIME (CHemical Th+U-total Pb Isochron Method) ages and uncertainties were calculated using the mathematical formulations of [32] and the regression functions of IsoplotR [33]. The accuracy of U+Th-total Pb dating is contingent upon the occurrence of negligible amounts of common Pb in the dated mineral. Its influence on U+Th-Pb ages is readily illustrated on isotopically dated monazite-(Ce) and xenotime-(Y) (e.g. [34,35], in which the ^{204}Pb content is typically less than 1 weight-% of the total Pb. This small common Pb abundance contributes only hundreds to thousands of years for Paleozoic phosphates, well within the overall analytical uncertainties. Hence, any minor common Pb is ignored in the U+Th-total Pb age computation in this study [36]. No excess or deficit ^{230}Th corrections was made for the (U+Th)-total Pb monazite-(Ce) and xenotime-(Y) ages. Any such effects are thought to be insignificant for the age range of interest here.

4. Results

4.1. Sampling and Petrography

The dated sample (lab no.1457) was taken from a mineralized carbonate vein located at the confluence of the Kisgyör tributary to the Belcina river (Figures 1, 2; 46°46'37.47" N / 25°41'26.27" E).

The sample is very heterogeneous in composition. Strongly mineralized domains (Figure 3a,b) are comparably coarse-grained with crystal sizes around 0.5 mm - 10 mm. Macroscopically the

Preprints (www.preprints.org) | NOT PEER-REVIEWED | Posted: 5 May 2023 doi:10.20944/preprints202305.0299.v1

composition is approx. 20 vol% monazite-(Ce), 30 vol% carbonate, 10 vol% plagioclase, 20 vol% thorite-thorogummite, the rest is xenotime-(Y), apatite, Fe oxides, and amphibole. The fabric is magmatic with no preferred crystal orientation, but brittle fracturing, especially of the monazite-(Ce), is ubiquitous. Non-mineralized domains (Figure 3c, d) are strongly brecciated with angular coarse-grained (0.5 mm - 5 mm) carbonate - K-feldspar - apatite ± white mica clasts in a fine-grained (< 0.1 mm) matrix of presumably identical composition. Sub-millimeter thick carbonate veinlets cross-cutting the domains are frequent.

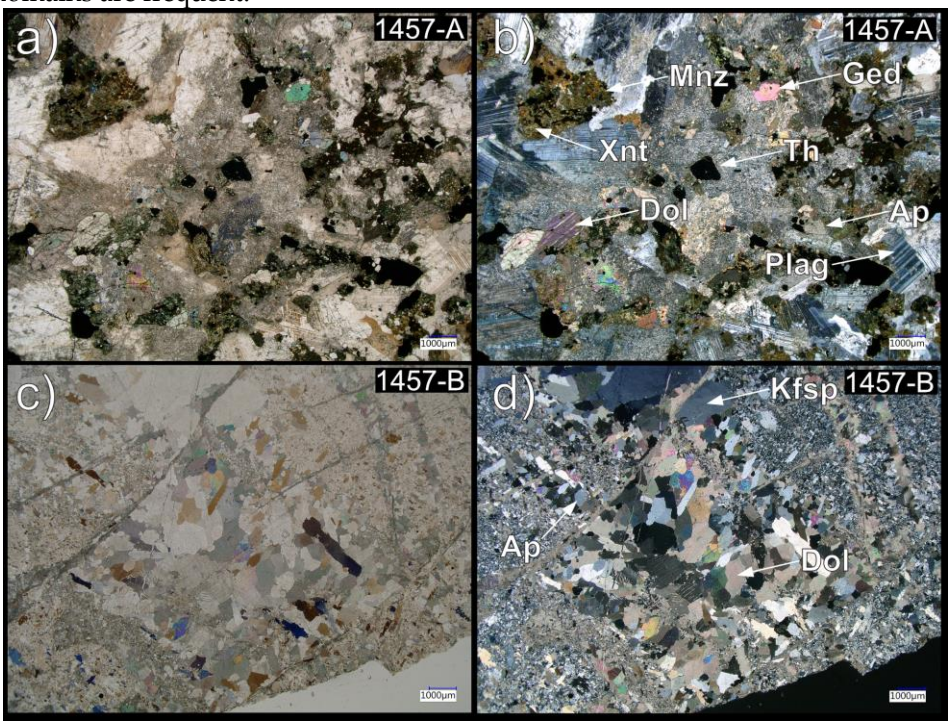

Figure 3. Thin section images of the Belcina carbonate mineralized vein sample. The sample can be divided in a coarse-grained part (1457-A) and a brecciated part (1457-B). Mineral phases identified by optical microscopy are labelled. The fine-grained aggregates, often forming pseudomorphoses, are only to be characterized by BSE or EMP analyses and are not labelled. All mineral data presented herein is from 1457-A. (**a**) 1457-A plane-polarized light and (**b**) crossed-polarized light. (**c**) 1457-B plane-polarized light and (**d**) crossed-polarized light.

4.2. Phosphate Morphology and Zonation

Based on assemblage and texture three different types of monazite-(Ce) and xenotime-(Y) occurrences can be distinguished in the mineralized parts of the investigated sample.

4.2.1. Monazite-(Ce)

- Type 1 monazite-(Ce) (mnz1) is rock-forming making up ca. 20 vol% of the rock. It either forms xenomorphic to hypidiomorphic aggregated mineral clusters of ca. 1 cm size or independent 100 µm - 500 µm sized crystals. It also is found as (relict) cores in type 2 monazite-(Ce) (Figures 4a,b,d and 5a).

Preprints (www.preprints.org) | NOT PEER-REVIEWED | Posted: 5 May 2023 doi:10.20944/preprints202305.0299.v1

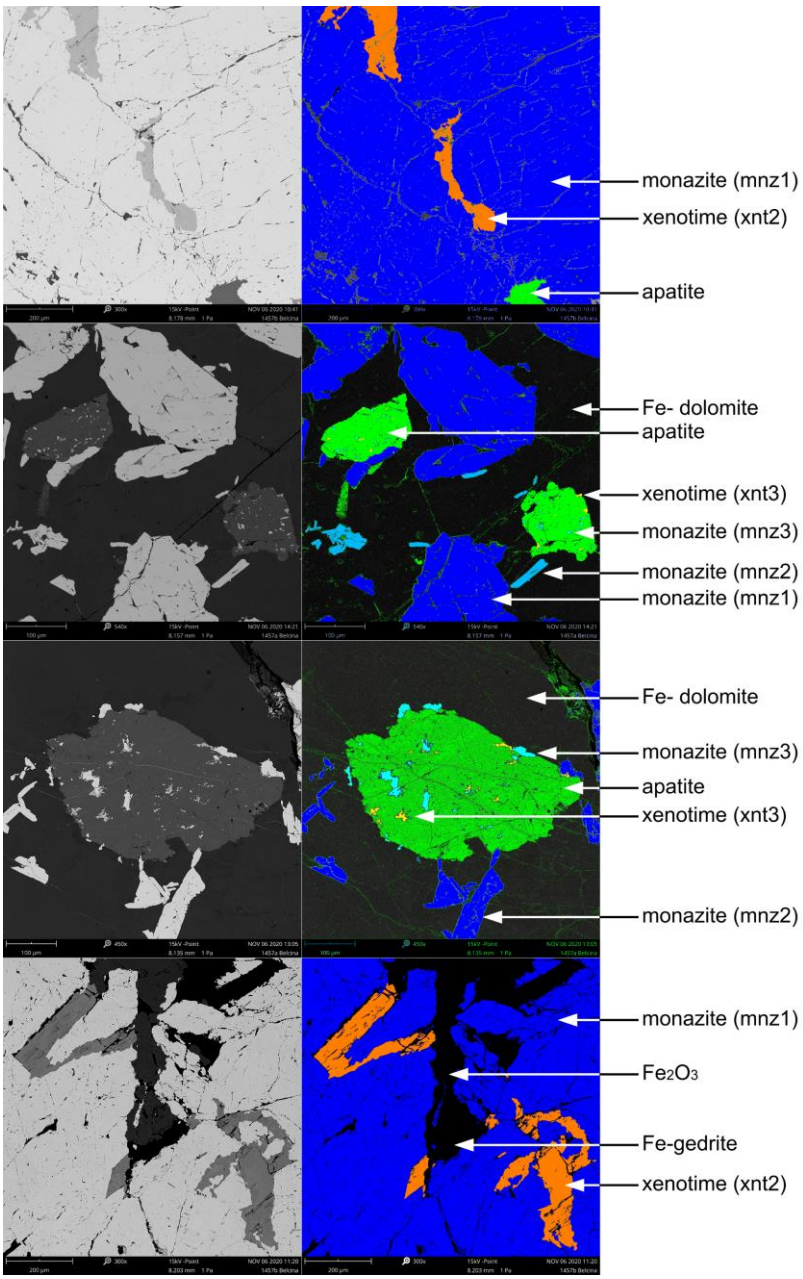

Figure 4. True and false-color backscattered electron images of the Belcina carbonate mineralized vein sample 1457 showing the different mineral parageneses and assemblages. Due to the reduced contrast resolution of these images xnt1 is not visible but is situated in the cores of the xnt2 crystals (also see Figure 6).

Preprints (www.preprints.org) | NOT PEER-REVIEWED | Posted: 5 May 2023 doi:10.20944/preprints202305.0299.v1

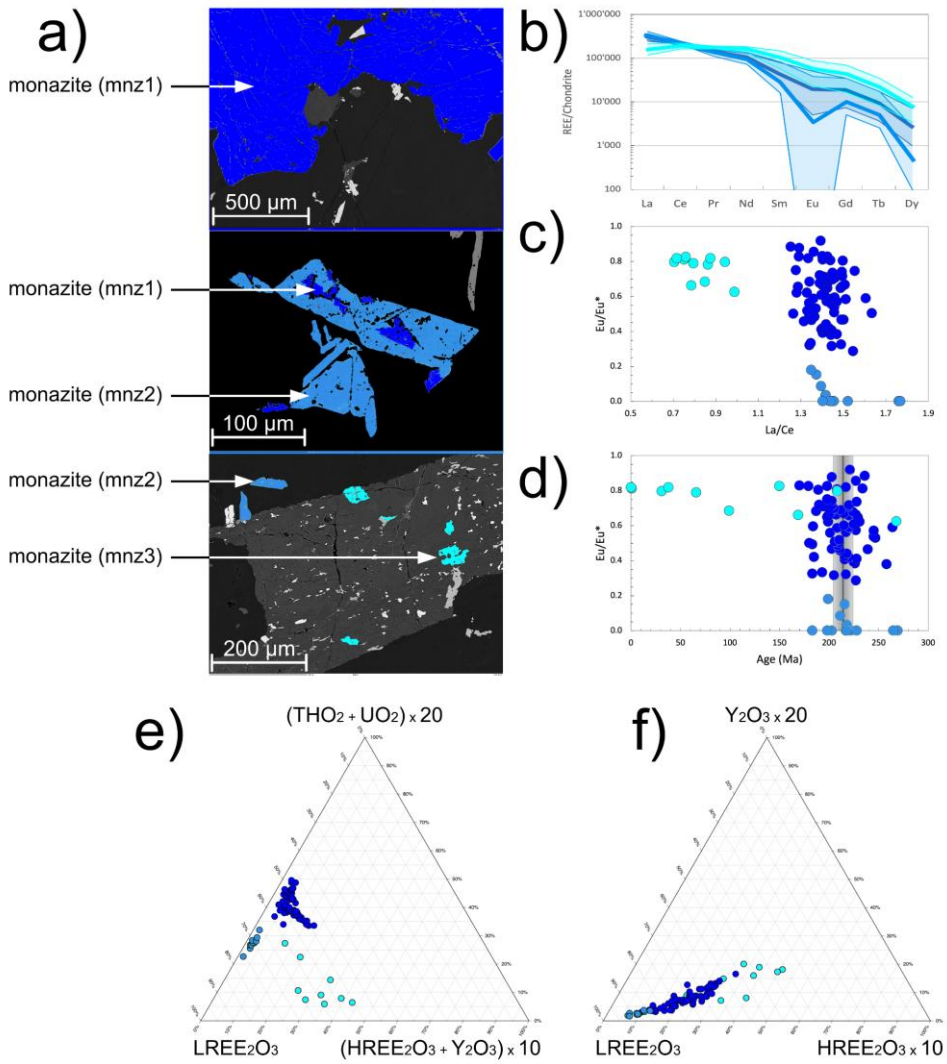

Figure 5. BSE images and chemistry of monazite-(Ce) from the Belcina carbonate mineralized vein sample 1457 (Table S1). (**a**) False color BSE images of the three characteristic textural monazite-(Ce) occurrences; (**b**) Normalized REE diagram using normalization values from [37]. The blue-shaded areas define the overall variation in REE contents. The thick blue lines denote the average REE composition of the three textural monazite-(Ce) types. (Note: The heavy REEs Ho to Lu are not shown as these were not determined due to EMP analytical limitations); (**c**) La/Ce versus Eu anomaly diagram depicting the diverse chemical composition of the three textural monazite-(Ce) types; (**d**) Age versus Eu anomaly diagram demonstrating that with the exception of a number of mnz3 analyses all dated monazite-(Ce) spots define the gray age interval of ca. 215 ± 6 Ma (2 standard deviations); (**e**) $LREE_2O_3$ versus $HREE_2O_3$+Y_2O_3 versus THO_2+UO_2 ternary diagram demonstrating that the different chemical compositions of the three monazite-(Ce) types. The general trend from mnz1 to mnz3 is a decrease in actinide content and a strong increase in the xenotime-(Y) component from mnz2 to mnz3 monazites. Mark the two linear trends seen in the mnz1 data; (**f**) REE_2O_3 versus $HREE_2O_3$ versus Y_2O_3 ternary diagram showing an overall pseudo-linear increase in the xenotime-(Y) component. Only by the distinction of the three textural monazites-(Ce) types it becomes evident that this is not a simple chemical trend (as is easily demonstrated in Figure 5e). For a more detailed discussion see text.

- Type 2 monazite-(Ce) (mnz2) forms independent small crystals (< 200 µm), always enclosed by Fe-dolomite (Figure 4c) and hypidiomorphic to idiomorphic in shape, often elongated (Figure 4b,c and 5a).

Preprints (www.preprints.org) | NOT PEER-REVIEWED | Posted: 5 May 2023 doi:10.20944/preprints202305.0299.v1

- Type 3 monazite-(Ce) (mnz3) is mostly found as inclusions in apatite or sometimes bordering apatite, tens of microns in size, and randomly oriented (Figures 4b,c and 5a). It is xenomorphic to hypidiomorphic in shape. Grain boundaries of mnz3 towards the host apatite are either straight and crystallographically oriented or lobate.

4.2.2. Xenotime-(Y)

- Type 1 xenotime-(Y) (xnt1) is only present as distinct domains in the cores of type 2 xenotime-(Y) (Figure 6a). It can only be identified by mineral chemical means and not texturally (see below).

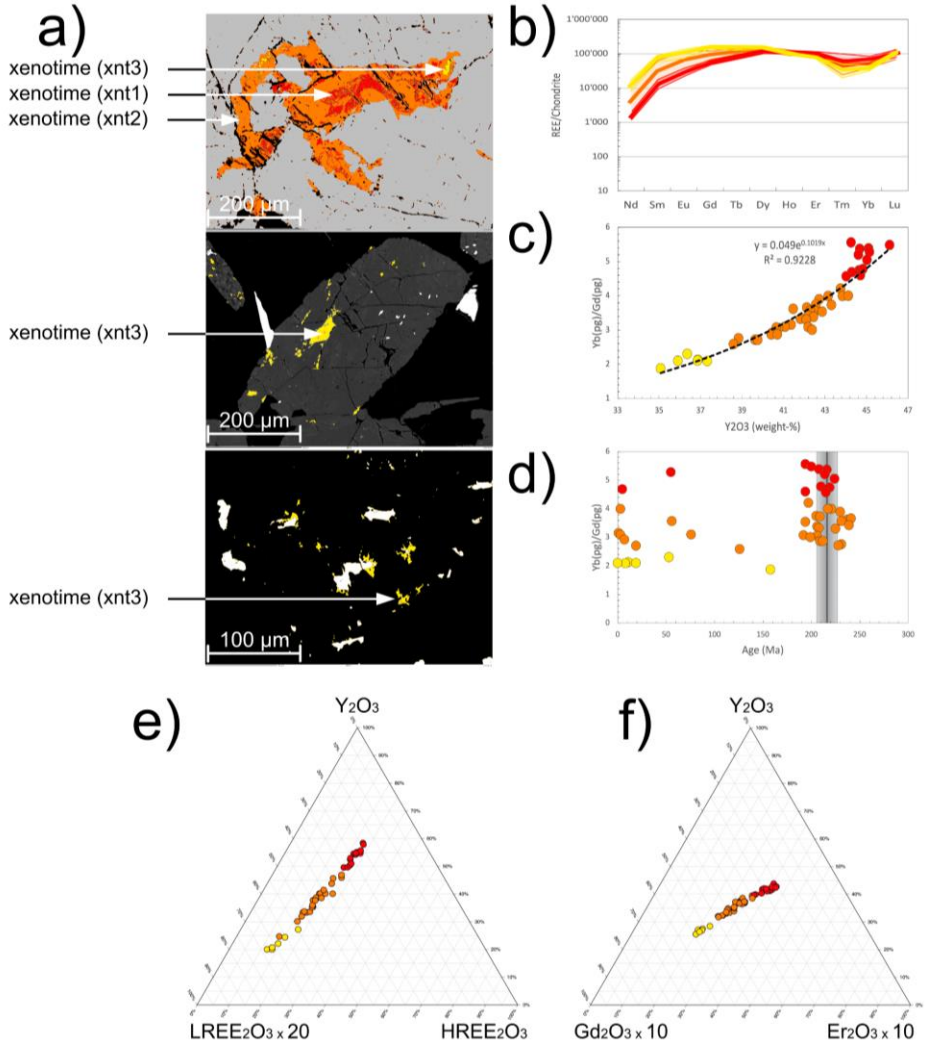

Figure 6. BSE images and chemistry of xenotime-(Y) from the Belcina carbonate mineralized vein sample 1457 (Table S2). (**a**) False color BSE images of the three characteristic textural xenotime-(Y) occurrences; (**b**) Normalized REE diagram (normalization values are from [37]. The red- to yellow-shaded areas define the overall variation in REE contents. The thick red-yellow lines denote the average REE composition of the three textural xenotime-(Y) types. (Note: The light REEs La to Pr are not shown as these were not determined due to EMP analytical limitations); (**c**) Plot of Y_2O_3 versus the ratio of the isomorphous mixtures of the paragenetic groups of [38]: Yb(pg) = (Y_2O_3 + Ho_2O_3 + Er_2O_3 + Yb_2O_3 + Lu_2O_3 + Nd_2O_3); Gd(pg) = (Gd_2O_3 + Tb_2O_3 + Dy_2O_3 + Eu_2O_3 + Sm_2O_3). From textural type 1 to type 3 a non-linear decrease in Y_2O_3 content going hand in hand with a decrease in the Yb(pg)/Gd(pg) is evident. The same REE trend can be seen in Fig. 6b by the cross-over in the mean REE composition at Ho; (**d**) Age versus paragenetic group ratio diagram demonstrating that irrespective of the chemical composition and with the exception of a number of analyses all type 1 and type 2 xenotimes-(Y) ages define the gray age interval of ca. 216 ± 9 Ma (2 standard deviations). Apparent ages of type 3 xenotimes-(Y) are all younger than 180 Ma; (**e**) $LREE_2O_3$ versus $HREE_2O_3$ versus Y_2O_3 ternary diagram demonstrating that the different chemical compositions of the three

Preprints (www.preprints.org) | NOT PEER-REVIEWED | Posted: 5 May 2023 doi:10.20944/preprints202305.0299.v1

xenotime-(Y) types. The linear trend from type 1 to type 3 xenotime-(Y) shows a strong increase in the monazite-(Ce) component and a minor increase in HREEs; (**f**) Gd_2O_3 versus Er_2O_3 versus Y_2O_3 ternary diagram showing an overall linear increase in Gd_2O_3 at constant Er_2O_3/Y_2O_3. For a more detailed discussion see text.

- Type 2 xenotime-(Y) (xnt2) forms a characteristic mineral assemblage with mnz1 within which it forms skeletal inclusions of > 100 μm size (Figures 4a,d and 6a). Xnt2 is never found as independent crystals. Grain boundaries of the xenotime-(Y) towards the host monazite-(Ce) are either straight and crystallographically oriented or lobate. The xnt2 does not show any preferred orientation within the host but is often related to fractures in mnz1.

- Type 3 xenotime-(Y) (xnt3), is tens of microns in size, mainly found as inclusions in apatite, seldomly in xnt2, and randomly oriented (Figures 4b,c and 6a). It is xenomorphic to hypidiomorphic in shape. Grain boundaries of xnt3 towards the host apatite are either straight and crystallographically oriented or lobate. In the appearance xnt3 is identical to mnz3.

4.3. Phosphates Chemistry

All REE concentrations (Tables 1 and 2) are either reported as REE_2O_3 weight-% or μg/g or as REE concentrations normalized to the chondrite values of [37].

Eu and Tm anomalies are calculated as: $(Eu/Eu^*)_N = Eu_N/(Sm_N*Gd_N)^{0.5}$, $(Tm/Tm^*)_N = Tm_N/(Er_N*Yb_N)^{0.5}$. The paragenetic groups in xenotime-(Y) of [38] are calculated as $Yb_{(pg)} = (Ho_2O_3 + Er_2O_3 + Yb_2O_3 + Lu_2O_3 + Nd_2O_3)$ and $Gd_{(pg)} = (Gd_2O_3 + Tb_2O_3 + Dy_2O_3 + Eu_2O_3 + Sm_2O_3)$.

4.3.1. Monazite-(Ce)

Type 1 monazite-(Ce) (mnz1): The average REE_2O_3 content is 65.3 weight%. The average $(La/Ce)_N = 1.42$, $(La/Dy)_N = 202$, $Eu/Eu^* = 0.66$ (Figure 5b,c). In $LREE_2O_3$ - ($HREE_2O_3$+Y_2O_3) - (ThO_2 + UO_2) space two trends are present (Figure 5e):

- trend 1 showing a relative actinide enrichment at constant xenotime-(Y) component;
- trend 2 showing enrichment in the xenotime-(Y) component at constants actinides.

Trend 1 is vertical on trend 2. Overall, the REE patterns of mnz1 closely resemble those of average metamorphic monazite-(Ce) and to a lesser extent hydrothermal monazite-(Ce) with some MREE enrichment (Figure 7a; Table S1).

Preprints (www.preprints.org) | NOT PEER-REVIEWED | Posted: 5 May 2023 doi:10.20944/preprints202305.0299.v1

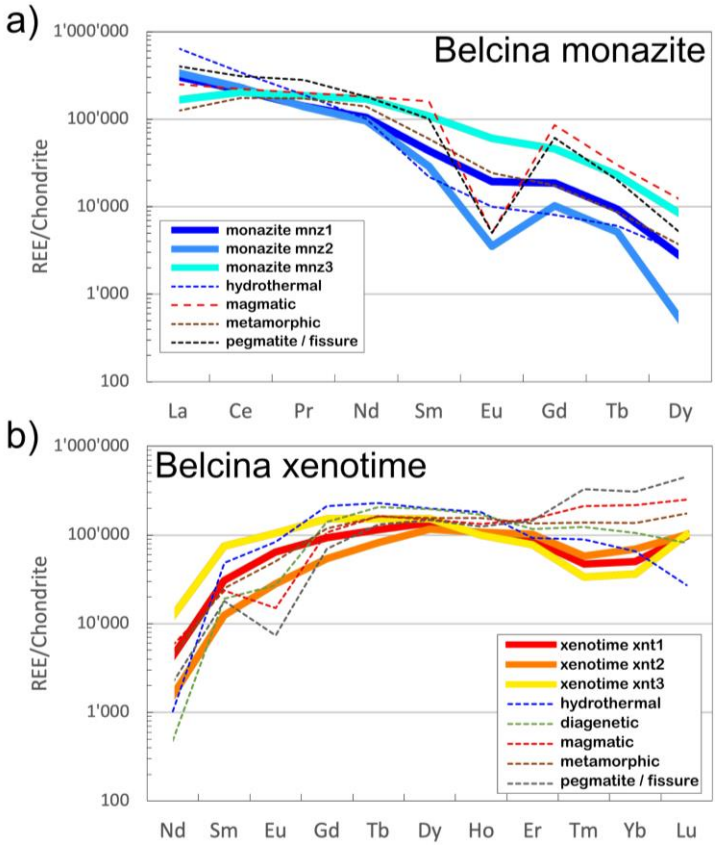

Figure 7. Chondrite normalized REE plots showing a comparison with the mean chondrite normalized REE literature values of hydrothermal, magmatic, metamorphic and pegmatite monazite-(Ce) and xenotime, respectively. Due to detection limit restrictions of the EMP analyses only the La-Dy data for monazite-(Ce) and the Nd-Lu data for xenotime-(Y), respectively, are available. (**a**) Monazite-(Ce): mnz1 and mnz3 follow a hydrothermal trend, to a lesser extent a metamorphic one, albeit at somewhat higher absolute concentrations of the MREE and HREE. Both trends are characterized with having only a small negative Eu anomaly (0.66 and 0.84, respectively). Mnz2 is not following this picture as having a marked negative Eu anomaly (0.09) more aking to a magmatic or pegmatitic origin. Normalization values are from [37]. (**b**) Xenotime-(Y): xenotime-(Y) shows an increase in LREE and MREE from xnt1 to xnt3, a cross-over of the trend at Ho and a corresponding decrease in the heaviest REEs (Er-Lu) from xnt1 to xnt3. Xnt1 has s very small positive Eu anomaly, xnt2 has none, whereas xnt3 has a small negative one. Compared to the mean trends from literature the Belcina xenotime-(Y) are strongly enriched in Nd and strongly depleted in Tm and Yb. Otherwise, they follow a trend similar to the trend of hydrothermal xenotimes-(Y) and less the one for metamorphic xenotime. Notably is the enrichment of all three xenotime-(Y) types in Lu. For further discussion see the text.

Type 2 monazite-(Ce) (mnz2): The average REE_2O_3 content is 64.5 weight%. The average $(La/Ce)_N$ = 1.46, $(La/Dy)_N$ = 152'757, Eu/Eu* = 0.09 (Figure 5b,c). Mnz2 is depleted in MREE and HREE compared to mnz1 (Figure 5b). In $LREE_2O_3$ - ($HREE_2O_3$+Y_2O_3) - (ThO_2 + UO_2) space one trend showing varying actinide enrichment at constant xenotime-(Y) component is visible (Figure 5e). This trend runs parallel the mnz1 trend 1 albeit at lower (ThO_2 + UO_2)/$LREE_2O_3$ ratios. The mean mnz2 REE pattern runs parallel the average hydrothermal monazite-(Ce) REE trend but with a more pronounced negative Eu anomaly and a LREE depletion (Figure 7a).

Type 3 monazite-(Ce) (mnz3): The average REE_2O_3 content is 64.1 weight%. The average $(La/Ce)_N$ = 0.82, $(La/Dy)_N$ = 25, Eu/Eu* = 0.84 (Figure 5b,c). Compared to the two former, monazite-(Ce) varieties mnz3 is depleted in La and Ce and strongly enriched in MREE and HREE (Figure 5b,c), (Figure 7a). In the $LREE_2O_3$ - ($HREE_2O_3$+Y_2O_3) - (ThO_2 + UO_2) space no specific trend is perceptible,

Preprints (www.preprints.org) | NOT PEER-REVIEWED | Posted: 5 May 2023 doi:10.20944/preprints202305.0299.v1

but compared to mnz1 and mnz2 the relative actinides contents are lowered. The mean mnz3 REE pattern runs parallel the mnz1 one but with a ca. five-fold MREE+HREE enrichment.

On the $LREE_2O_3$ - $HREE_2O_3$ - Y_2O_3 ternary plot the three monazite-(Ce) varieties define one constant trend (Figure 5f) from purer mnz2 to mnz3 with higher xenotime-(Y) component and a constant $Y_2O_3/HREE_2O_3$ ratio. All five compositional trends in the $LREE_2O_3$ - ($HREE_2O_3$+Y_2O_3) - (ThO_2 + UO_2) (Figure 5e) and $LREE_2O_3$ - $HREE_2O_3$ - Y_2O_3 spaces (Figure 5f) are not related to any particular textural position in the monazite-(Ce)s.

Principal component analysis (Figure 8) using La, Ce, P, Y, Si, Al, K, Ca, S, Fe, Sr, Pr, Nd, Sm, Eu, Gd, Dy, U, and Th shows that 56.1% of the total observed variance in the monazite-(Ce) chemistry is attributed to Dim1 and Dim2 (Figure 8a). Dim1 (43.7% of total variance) is formed by the positive correlation of Pr, Nd, Sm, Eu, Gd, Dy, Y, and P, whereas La and Ce are negatively correlated with the former elements. Dim2 (12.4% of total variance) is dominated by strongly positively correlated Ca, Si, and Fe and to a lesser amount by Th and Sr. U, S, Al, K do not contribute significantly to the compositional variance (Figure 8b). Notable, very strong positive correlations of Th with Sr, and Ca with Fe are evident.

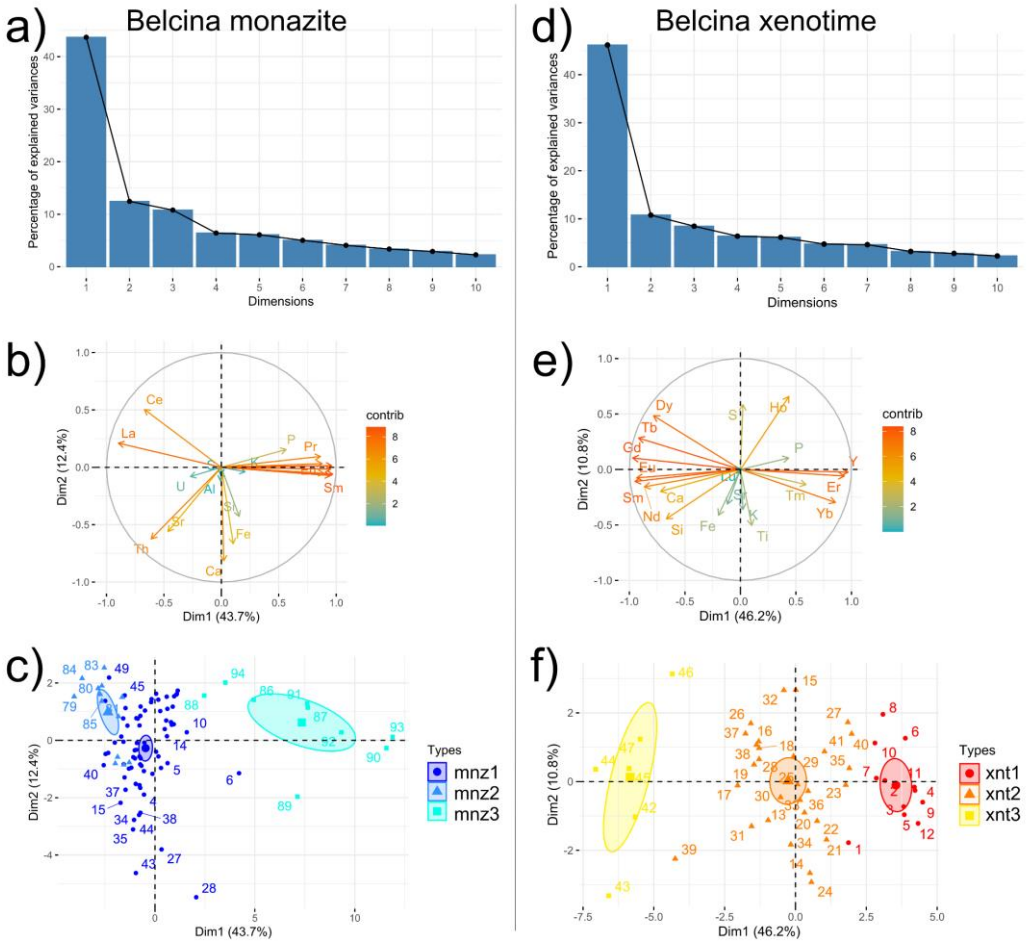

Figure 8. Principal component analysis (PCA) of the Belcina carbonate mineralized vein sample 1457. Elements used for the monazite-(Ce) PCA are: Y, Si, Al, K, Ca, P, S, Fe, Sr, La, Ce, Pr, Nd, Sm, Eu, Gd, Dy, U, Th. Elements used for the xenotime-(Y) PCA are: Si, Ti, Ca, S, Ho, Y, Sr, K, P, Fe, Nd, Sm, Eu, Gd, Tb, Dy, Er, Tm, Yb, Lu. All other analyzed elements (Tables 1, 2) were not included in the PCA. (**a**) Monazite-(Ce); (**d**) xenotime-(Y): Scree plots showing the 10 most important variance components (eigenvalues). Components (principal dimensions) Dim1 and Dim2 allow to statistically characterize the three monazite-(Ce) types found in the sample adding up to > 50 % of the total variance, whereas components 1 to 3 make up for more than 65% of the total variance. (**b**) Monazite-(Ce); (**e**) xenotime-(Y): Polar plots showing the element contribution to the most important variance dimensions Dim1 and Dim2. The length and coloring of the element vectors indicate their relative variance contribution. Parallel vectors indicate a positive correlation of the respective element concentrations whereas anti-

 doi:10.20944/preprints202305.0299.v1

parallel vectors indicate a negative correlation. (**c**) Monazite-(Ce); (**f**) xenotime-(Y): Dim1 - Dim2 scatter plot of all analyses delineating the three different phosphate types, their mean value and a 1-sigma uncertainty ellipse.

Dim1 internal variance is the strongest for mnz3 (ca. 20%), whereas mnz1 and mnz2 show the same amount of Dim1 variance. Dim2 variance is the strongest in mnz1 (ca. 8%), followed by mnz3 and mnz2 (Figure 8c).

4.3.2. Xenotime-(Y)

Type 1 xenotime-(Y) (xnt1): The average REE_2O_3 content is 64.8 weight%. The average $(Nd/Lu)_N$ = 0.02, Eu/Eu* = 1.08, Tm/Tm* = 0.69 (Figure 6b). The average paragenetic group values are $Yb_{(pg)}$ = 53.1, $Gd_{(pg)}$ = 10.5, $Yb_{(pg)}/Gd_{(pg)}$ = 5.06 (Figure 6c,d). The mean xnt1 REE pattern runs parallel the average hydrothermal/metamorphic xenotime-(Y) REE trends but with a positive Eu anomaly, a pronounced negative Tm anomaly and Lu enrichment (Figure 7b; Table S2).

Type 2 xenotime-(Y) (xnt2): The average REE_2O_3 content is 64.5 weight%. The average $(Nd/Lu)_N$ = 0.05, Eu/Eu* = 1.21, Tm/Tm* = 0.71 (Figure 6b). The average paragenetic group values are $Yb_{(pg)}$ = 49.1, $Gd_{(pg)}$ = 14.9, $Yb_{(pg)}/Gd_{(pg)}$ = 3.34 (Figure 6c,d). The mean xnt2 REE pattern also runs parallel the average hydrothermal/metamorphic xenotime-(Y) REE trends. It shows lower concentrations of Nd-Tb than xnt1 and higher Er-Lu than xnt1 but also the pronounced negative Tm anomaly and Lu enrichment of xnt1 (Figure 7b).

Type 3 xenotime-(Y) (xnt3): The average REE_2O_3 content is 64.1 weight%. The average (Nd/Lu)N = 0.13, Eu/Eu* = 0.98, Tm/Tm* = 0.64 (Figure 6b). The average paragenetic group values are Yb(pg) = 43.7, Gd(pg) = 20.9, Yb(pg)/Gd(pg) = 2.10 (Figure 6c, d). The mean xnt3 REE pattern also runs parallel the average hydrothermal/metamorphic xenotime-(Y) REE trends. It shows higher concentrations of Nd-Tb than xnt1 and xnt2 and the most pronounced negative Tm anomaly, Yb depletion and Lu enrichment (Figure 7b).

All three xenotime-(Y) types follow a well-defined exponential correlation of Y_2O_3 with $Yb_{(pg)}/Gd_{(pg)}$, xnt1 having the highest value and xnt3 the lowest. In contrast to this, no correlation of the xenotime-(Y) mineral chemistry, characterized by Yb(pg)/Gd(pg), with the (Th+U)-total Pb age is detectable (Figure 6d). On the $LREE_2O_3$ - $HREE_2O_3$ - Y_2O_3 ternary plot the three xenotime-(Y) varieties define one constant trend with a continuous increase of the REE_2O_3 concentration and of the monazite-(Ce) component from xnt1 to xnt3 (Figure 6e). On a Gd_2O_3 - Er_2O_3 - Y_2O_3 ternary plot the three xenotime-(Y) varieties also define a constant trend with a continuous increase of Gd_2O_3 at a virtual constant Er_2O_3/Y_2O_3 (Figure 6f).

Principal component analysis (Figure 8) using Y, P, Si, Ti, Ca, S, Ho, Sr, K, Fe, Nd, Sm, Eu, Gd, Tb, Dy, Er, Tm, Yb, and Lu shows that 57.0 % of the total observed variance in the xenotime-(Y) chemistry is attributed to Dim1 and Dim2 (Figure 8d). Dim1 (46.2% of total variance) is formed by the positive correlation of Y, Yb, Er, and to a lesser extent P and Tm, whereas the other REE-Ca-Si are negatively correlated with the former. Dim2 (10.8% of total variance) is dominated by S, K, Ti, Fe, and to a lesser amount by K and Sr (Figure 8e). There is a the very strong positive correlation of Si and Ca (cheralite-huttonite substitution) and no positive correlation of P and Ca. Lu does not contribute to Dim1 or Dim2. Ho shows a significant aberrant behavior when compared to the other REEs showing a strong positive correlation of Dim1 with Dim2.

The three textural xenotime-(Y) types can also be clearly resolved by their Dim1-Dim2 values (Figure 8f). The mean values and their 1-sigma confidence limits show that the three types can be distinguished solely on the basis of Dim1, i.e., their REE systematics. Dim2 (Ti, K, Fe, Sr, S) do not discriminate the xenotime-(Y) types. As has been shown by the element - element correlations xnt1 shows the purest xenotime-(Y) composition, i.e., the strongest positive Dim1 component, whereas xnt3 shows the highest amount of LREE and MREE (in parts as monazite-(Ce) component) contribution having strongly negative Dim1 values. The xnt3 composition is dominated by the Dim2 components, i.e., the non-stoichiometric elements Ti, K, Fe, Sr, and S.

Preprints (www.preprints.org) | NOT PEER-REVIEWED | Posted: 5 May 2023 doi:10.20944/preprints202305.0299.v1

Dim1 internal variance is the strongest for xnt2 (ca. 6%), whereas xnt1 and xnt3 show the same amount of Dim1 variance (ca. 3%). Dim2 variance is largest in xnt2 and xnt3 (ca. 6%), lest in xnt1 (Figure 8f).

4.4. EMP U+Th-Total Pb Ages

4.4.1. Monazite-(Ce)

The monazite-(Ce) EMP U+Th-total Pb age data are presented in Figures 9 and 10 and Table S1.

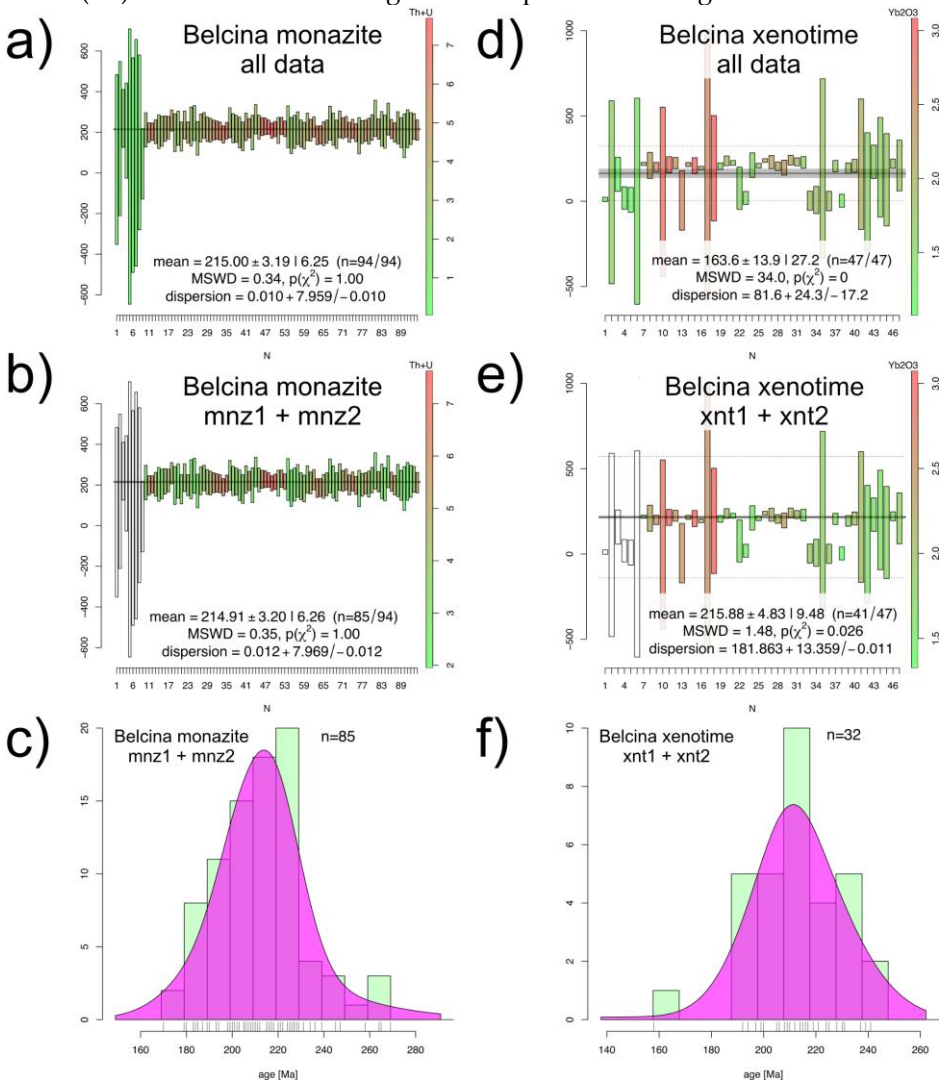

Figure 9. Belcina monazite-(Ce) and xenotime-(Y) U+Th-total Pb spot ages (Tables S1, S2). (**a**) Histogram of all 94 monazite-(Ce) spots. (**b**) Histogram of the 85 spots from mnz1 and mnz2. (**c**) Kernel density function of the 85 spots from mnz1 and mnz2 showing a near perfect normal distribution of the U+Th-total Pb spot ages. (**d**) Histogram of all 47 xenotime-(Y) spots. (**e**) Histogram of the 41 spots from xnt1 and xnt2. (**f**) Kernel density function of the 32 most precise spots from xnt1 and xnt2 showing a near perfect normal distribution of the U+Th-total Pb spot ages. The U+Th-total Pb spot ages are color-coded according to the Th/U ratio. The mean ages are weighted means without any outlier detection. The kernel density functions are calculated with a kernel density bandwidth of 7 Ma and the adaptive KDF option of IsoplotR [33].

Preprints (www.preprints.org) | NOT PEER-REVIEWED | Posted: 5 May 2023 doi:10.20944/preprints202305.0299.v1

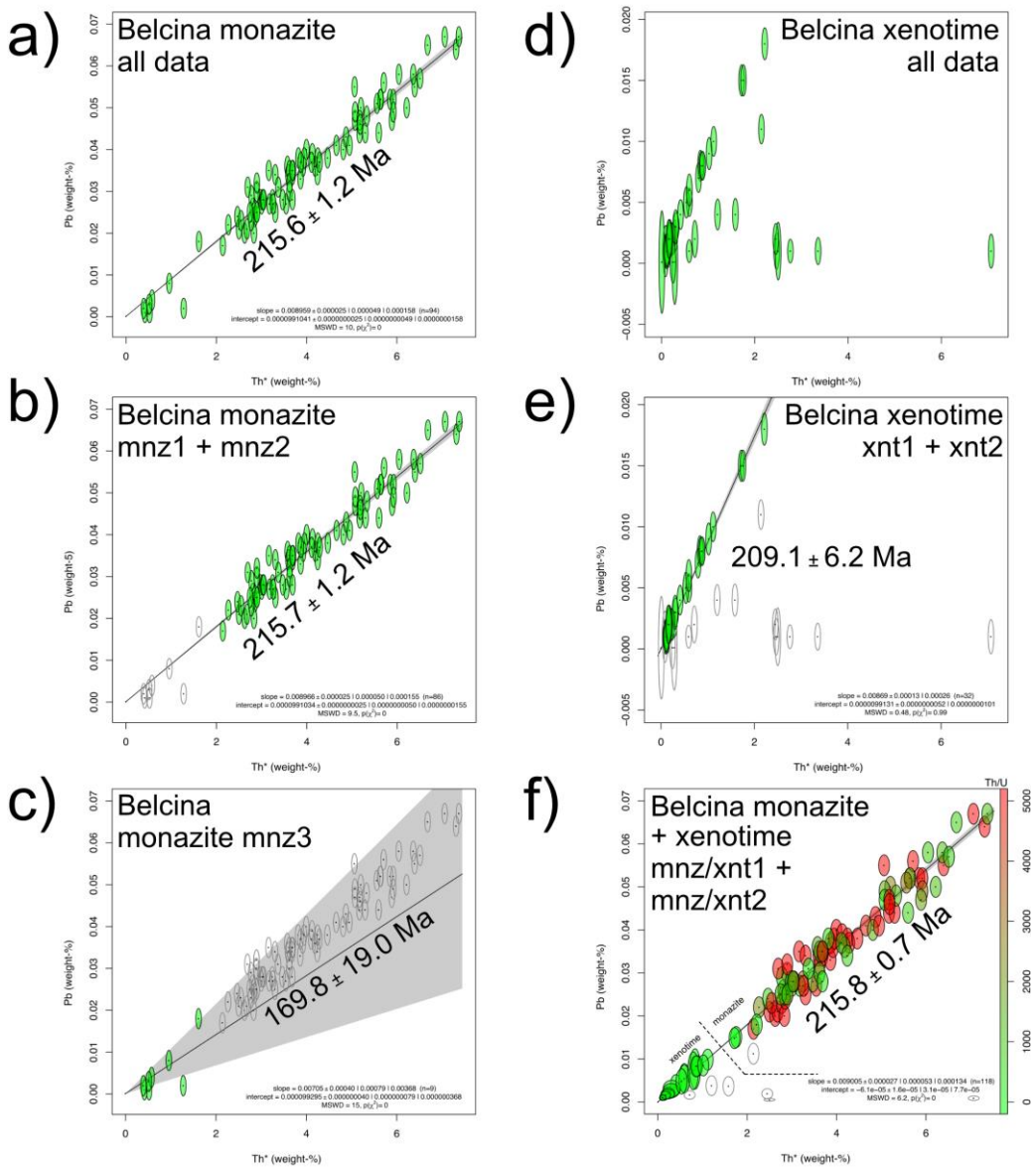

Figure 10. Belcina monazite-(Ce) and xenotime-(Y) U+Th-total Pb CHIME (CHemical Isochron Method) ages [32] (Tables S1, S2). (**a**) Monazite-(Ce) CHIME age calculated for all 94 spots. (**b**) Monazite-(Ce) CHIME age calculated for the 85 mnz1 and mnz2 spots. (**c**) Monazite-(Ce) CHIME age calculated for 9 mnz3 spots. (**d**) Xenotime-(Y) CHIME diagram for all 47 spots. (**e**) Xenotime-(Y) CHIME age calculated for the 32 xnt1 and xnt2 spots. (**f**) CHIME diagram showing the combination of mnz1+mnz2+xnt1+xnt2. The spots are color-coded according to the Th/U ratio.

A total 97 of spots were analyzed on 11 crystals. The UO_2 contents vary from below the EMP detection limit to 110 µg/g with an average of 21 µg/g. ThO_2 varies from 0.29 weight-% to 7.35 weight-% with an average of 3.75 weight-%. PbO contents vary from below the EMP detection limit to 670 µg/g with an average of 340 µg/g. Out of the 97 analyzed spots 94 delivered analytically useful ages in the range of 0 ± 113 Ma (1457b-04-01_mnz_1) to 717 ± 793 Ma (1457b-03-02-mnz_1). The weighted mean age of all 94 spots is 215.0 ± 6.3 Ma (Figure 9a). Compared to mnz1 and mnz2 the mnz3 ages (9 spots) show a strongly reduced analytical precision due to the lower U and Th contents (Figure 5e). The weighted mean age of the mnz3 spots is accordingly 238.4 ± 108.9 Ma (not shown). Taking only mnz1 and mnz2 spots into account (85 spots) the weighted mean age is 214.9 ± 6.3 Ma (Figure 9b). Both ages are identical within the 2 standard deviation uncertainties.

The mnz1 CHIME age calculate by a free regression is 216.7 ± 4.3 Ma (MSWD=10.0). When calculated by a regression forced through the origin it is 215.4 ± 1.3 Ma (MSWD=9.8). Mnz2 CHIME

 doi:10.20944/preprints202305.0299.v1

ages are, respectively, 204.3 ± 11.5 Ma (MSWD=8.1) and 218.2 ± 3.4 Ma (MSWD=7.9). Mnz3 CHIME ages are, respectively, 248.6 ± 40.4 Ma (MSWD=14.0) and 169.8 ± 19.0 Ma (MSWD=15.0, Figure 10c) and). Combining mnz1 and mnz2 results in a forced regression CHIME age of 215.7 ± 1.2 Ma (MSWD=9.5; Figure 10b). Combining all 94 monazite-(Ce) analyses a CHIME age of 215.6 ± 1.2 Ma (MSWD=10.0; Figure 10a) when forced through the origin is found.

All intercepts of the free regression CHIME calculations pass within the 2-sigma uncertainty the origin justifying the use of the forced regression CHIME age for the further discussion [31,39].

No inheritance visible.

- Mnz3 show reduced precision due to the comparable low actinide contents and the resulting low Pb contents.

4.4.2. Xenotime-(Y)

The xenotime-(Y) EMP (U+Th)-total Pb age data are presented in Figures 9, 10 and Table S2.

A total 47 of spots were analyzed. UO_2 contents vary from below the EMP detection limit to 130 µg/g with an average of 100 µg/g. ThO_2 varies from below the EMP detection limit to 770 µg/g with an average of 105 µg/g. PbO contents vary from below the EMP detection limit to 90 µg/g with an average of 70 µg/g.

All 47 spots delivered useful ages in the range of 0 ± 617 Ma (1457b-04-02_xnt_04) to 241 ± 29 Ma (1457b-02-02_xnt_12). The weighted mean age of all 47 spots is 163.6 ± 27.2 Ma (Figure 9d). Taking only xnt1 and xnt2 into account (41 spots) the weighted mean age is 215.9 ± 9.5 Ma (Figure 9e).

CHIME age systematics are: Xnt1 ages are, respectively, 204.1 ± 9.3 Ma (MSWD=0.51; free regression) and 208.7 ± 6.5 Ma (MSWD=0.56; forced regression). Xnt2 CHIME ages are, respectively, 208.7 ± 34.3 Ma (MSWD=0.25) and 214.9 ± 24.9 Ma (MSWD=0.26). The xnt3 data do not allow to calculate a CHIME age (Figure 10d). Combining xnt1 and xnt2 results in a CHIME age of 204.6 ± 8.9 Ma (MSWD=0.43) and 209.1 ± 6.2 Ma (MSWD=0.48;Figure 10e), respectively. All intercepts of the free regression CHIME calculations are within the 2-sigma uncertainty of the origin justifying the use of the forced regression CHIME age for the further discussion [31,39]. No inheritance visible.

Combining the monazite-(Ce) (mnz1, mnz2) and xenotime-(Y) (xnt1, xnt2) data, a forced regression CHIME age of 215.9 ± 1.3 Ma (MSWD=6.2, Figure 10f) results.

5. Discussion

5.1. Phosphate Chemistry and Textures

The phosphates of the Belcina carbonate REE mineralized veins, together with carbonate, thorite, thorogummite and plagioclase, are rock-forming. The investigated sample though is somewhat aberrant in its modal composition, as in general in the Belcina veins thorite, thorogummite, zircon and xenotime-(Y) abundances are higher and monazite-(Ce) is less common than in our sample.

We choose the sample based on the fact that the seemingly straight-forward approach of dating the rock-forming and usually most abundant thorite and/or thorogummite is not practicable. Both minerals are strongly prone to accumulate considerable amounts of metamictization thus most certainly rendering any dating attempt unsuccessful. And in contrast to the observations of [4,8], zircon is not present in all our Belcina samples. Additionally, [8] states that the zircon from the Jolotca and Belcina mineralizations has a different chemical composition. In the Belcina samples zircon tends to show a very high ThO_2 content (>20 weight-%), thus rendering it to be highly metamict, while in the Jolotca samples the ThO_2 content generally is low (<1 weight-%). Obviously, any attempt to date zircon from the Belcina mineralize carbonate veins seems would not be successful. Consequently, for our geochronological investigations, we have chosen a sample which guaranteed the highest possibility of successfully dating monazite-(Ce) and xenotime-(Y) by in-situ U+Th-total Pb EMP analyses. As monazite-(Ce) is more convenient (higher Th content) for high-precision U+Th-total Pb EMP dating than xenotime-(Y) we have focused thereby on monazite-(Ce).

Preprints (www.preprints.org) | NOT PEER-REVIEWED | Posted: 5 May 2023 doi:10.20944/preprints202305.0299.v1

5.1.1. Common Features

Both phosphates show a specific three stage evolution depicted by both mineral chemistry and textures. A relative phosphate crystallization succession xnt1 > xnt2 > and/or + mnz1 > mnz2 > mnz3 + xnt3 + apatite can thus be derived.

Texturally, xnt1 is the oldest phosphate, only found as patchy domains and cores in the xnt2 crystals (Figure 6). We cannot unambiguously decide whether xnt1 is merely overgrown or actually replaced by xnt2. But in view of the characteristics of the chemical boundaries, xnt1 was likely first partially resorbed and then subsequently overgrown by xnt2. Within the SEM spatial resolution (ca. 2 µm) no transition of xnt1 to xnt2 is visible, supporting the above interpretation. Xnt2 on the other hand is only found within mnz1 and is the most abundant xenotime-(Y) type. Xnt2 is never in contact with apatite, Fe-dolomite or the Th silicates. It is however in contact with Fe_2O_3 and the Fe-gedrite.

The most abundant rock-forming phosphate is mnz1, making up ca. 20 vol% of the rock. It either forms xenomorphic to hypidiomorphic aggregated mineral clusters of ca. 1 cm size or independent 100 µm - 500 µm sized crystals. It also is found as (relict) cores in mnz2. The two chemical trends seen in $LREE_2O_3$ - ($HREE_2O_3$+Y_2O_3) - (ThO_2 + UO_2) space are not related to any textural patterns, especially the rock-forming mnz1 and the relict mnz1 cores in the mnz2 crystals cannot be distinguished chemically. This definitely speaks in favor of mnz2 having overgrown mnz1. The chemical trend 1 (Figure 5e) indicates a decrease in the actinide activity in the mineralizing fluid, whereas trend 2 is related to the contemporaneous growth of xnt2 (and xnt1?) thus reducing the fluid's HREE activity. Mnz2 always forms independent crystals of medium size and is always associated with Fe-dolomite. Chemically the two monazite-(Ce) types are similar, albeit mnz2 being somewhat REE richer and having a more pronounced Eu anomaly. But as with the xnt1-xnt2 pair (see below) the monazite-(Ce) types form chemically independent groups without any chemical transition between them. This strongly speaks in favor of an immediate change in the REE composition and activity of the mineralizing fluid after this has evolved over some time consciously in two phases leading to the observed two trends in mnz1. Xnt3 and mnz3 are always in contact with apatite and never found as isolated crystals. They are the least abundant phosphate types, forming only comparably small crystals and are interpreted, at least in parts, as exsolution products of apatite as a result of dissolution–reprecipitation processes during metasomatic alteration of the apatite: $(Ca+REE)_5(PO_4)_3$ -> $Ca_5(PO_4)_3$ + $(LREE)_5(PO_4)_3$ + $(HREE)_5(PO_4)_3$ (e.g. [17,40-42]). Such an origin of xnt3 and mnz3 is also substantiated by the fact that these show the highest number of impurities. The extended paragenetic succession of the Belcina phosphates is thus xnt1 > xnt2 (>)+ mnz1 + Fe_2O_3 + Fe-gedrite > mnz2 + Fe-dolomite > mnz3 + xnt3 + apatite.

5.1.2. Xenotime-(Y) Chemistry

The three xenotime-(Y) types are chemically independent as they show very distinct compositional features (Figures 6c, d, e) without any transition of one type to the other being visible. Each xenotime-(Y) type shows an individual chemical evolution exemplified for instance by the chemical trends seen in the $LREE_2O_3$ - $HREE_2O_3$ - Y_2O_3 or Gd_2O_3 - Er_2O_3 - Y_2O_3 spaces (Figure 6e, f). As xenotime-(Y) shows a decrease in the pure YPO_4-component from xnt1 to xnt3 with a concomitant increase in the monazite-(Ce) component. Notable is the very strong positive correlation of Si and Ca (cheralite-huttonite substitution) and the attribution of P only to xenotime-(Y) and not to apatite, as there is no positive correlation of P and Ca. The REE discrimination shown by the PCA can be correlated with the paragenetic groups:

- $Yb_{(pg)}$ = (Ho_2O_3 + Er_2O_3 + Yb_2O_3 + Lu_2O_3 + Nd_2O_3): All Dim1 positive and Dim2 negative with the exception of Nd which in Dim1 negative. Lu is not significant.

- $Gd_{(pg)}$ = (Gd_2O_3 + Tb_2O_3 + Dy_2O_3 + Eu_2O_3 + Sm_2O_3): All Dim1 negative and Dim2 positive with the exception of Sm which is negative in Dim2.

The aberrant behavior of Sm and Nd is attributed to the fact that both elements belong to the monazite-(Ce) component in xenotime-(Y) and thus should not be included in the paragenetic groups of xenotime-(Y).

 doi:10.20944/preprints202305.0299.v1

5.1.3. Monazite-(Ce) Chemistry

The three monazite-(Ce) types are chemically independent as they show very distinct compositional features (Figure 5c,d,e) without any transition of one type to the other being visible. But it is also important to state that each monazite-(Ce) type shows an individual chemical evolution exemplified for instance by the chemical trends seen in the $LREE_2O_3$ - ($HREE_2O_3$+Y_2O_3) - (ThO_2 + UO_2) space (Figure 5e). Strongly generalizing, an overall trend from purer monazite-(Ce)-Ce to monazite-(Ce) with a higher xenotime-(Y) and a lower actinide component is evident. But these trends are continuous.

This evolutionary succession is further substantiated by the PCA:

The three monazite-(Ce) types can also clearly be resolved by their PCA Dim1-Dim2 values, where Dim1 primarily stands for the REE variance, whereas Dim2 mainly reflects the cheralite ($CaTh[PO_4]$) – huttonite ($Th_2[SiO_4]$) substitutions.

The mean values and their 1-sigma confidence limits show that the three monazite-(Ce) types actually can be distinguished solely on the basis of Dim1 (REE, P) contributing to 43.7% of the total compositional variance. Dim2 (Ca, Si, Fe) does not discriminate the monazite-(Ce) types that significantly (12.4% variance). A significant apatite ($Ca_5[(PO_4)_3]$) component in mnz1 is not directly conceivable. Therefore all Ca has to reside in either the cheralite or some other not identified component. Mnz1 shows the highest variation in the amount of the cheralite-huttonite substitutions, whereas mnz3 shows the highest variation in the variability of the REE composition.

As has been shown by the element - element correlations mnz1 shows the purest monazite-(Ce) composition, i.e., the highest Dim1 component of the main-constituents LREE-P, whereas mnz3 shows the highest amount of non-main-constituents contribution.

In general, the variations in the crystal chemical compositions of the Belcina carbonate vein monazite-(Ce)s reveal that three different fractionations trends can be distinguished and that these trends are distinct for each textural monazite-(Ce) group. For instance, the xenotime-(Y) component decreases from mnz1 to mnz2, but increase in mnz3 to even higher values as in mnz2 (Figure 5e, f). These geochemical trends shows that the fluids from which the monazite-(Ce) crystallized had dissimilar and possibly not even related compositions.

5.1.4. Overall Interpretation

Although no systematic chemical zonations such as concentric growth zonations are visible in the investigated phosphates, we interpret all mineral chemistry data as reflecting growth conditions and not post-growth alteration. As such these mineral chemical characteristics are interpreted as giving evidence for mineral growth in at least three independent events with no transition of one event into the other being visible.

The xenotime-(Y) and monazite-(Ce) REE mineral chemistry definitely indicates a hydrothermal origin (Figure 7a,b). However, there are certain characteristics of the REE systematics which remain to be explained. One such feature is the prominent negative mnz2 Eu anomaly. Traditionally this is explained by plagioclase fractionation from the igneous source or the coeval growth of plagioclase in a magmatic melt system [43]. As the Belcina REE carbonate mineralization can be interpreted as a hydrothermal dominated magmatic system with plagioclase as a important phase, we can tentatively interpret mnz2 as crystallizing in the presence of plagioclase in as much as the possibly also coeval Fe-dolomite growth probably did not lead to the formation of a negative Eu anomaly in mnz2 [44]. Texturally mnz2 is not associated with any of the three xenotime-(Y) types. This is perfectly reflected in the absence of any marked Eu anomaly in the xenotime-(Y) which could be expected to be present if any of the xenotime-(Y) would be paragenetically associated with mnz2 or plagioclase.

Another interesting feature are the negative Tm and the positive Lu anomalies in the xenotime-(Y). Such anomalies have not been documented yet for hydrothermal xenotime-(Y). The only literature data suggestion the presence of a negative Tm anomaly in xenotime-(Y) comes from a sample from the peraluminous Ehrenfriedersdorf granite (Erzgebirge, Germany [45]). But this sample is missing the positive Lu anomaly present in the Belcina xenotime-(Y). On the other hand, pegmatitic xenotimes sometime show a positive Lu fractionation, albeit at far higher HREE concentrations

 doi:10.20944/preprints202305.0299.v1

(Figure 7b). But pegmatitic xenotime-(Y) also show a well-developed negative Eu anomaly, which obviously is not present in the Belcina xenotime-(Y). We propose that the observed HREE anomalies are related to a typical W-type tetrad effect in xenotime-(Y). In hydrothermal phosphates HREE tetrad effects are suggested to be caused by complexation in F-rich fluids [45-47]. As xnt3 is formed by the exsolution from fluor apatite, we assume the contemporary presence of such F-rich fluids in equilibrium with apatite having caused the tetrad effect in xnt3. But such a scenario would imply, that the xnt3 and mnz3 actually grew contemporaneously with apatite and that they thus were not the result of a post-growth exsolution from apatite as is commonly assumed in literature.

We thus propose the presence of at least three distinct mineral paragenesis indicative for a three-stage hydrothermal evolution of the REE carbonate mineralization:

a) xnt1 + xnt2 + mnz1
b) mnz2 + plagioclase
c) xnt3 + mnz3 + apatite + Fe-dolomite

The question arises whether the phosphate mineral chemistry can directly be correlated with the crystallization temperature. Such a relation has been found in a number of investigations [13,19,48,49]. If such a relation is applicable to the Belcina REE carbonate mineralization, the observed trends in the phosphate compositions would imply that the succession xnt1/xnt2/mnz1 to xnt3/mnz3/apatite/Fe-dolomite was formed during rising temperatures. But this interpretation cannot be unambiguous as the mineral chemistry of xnt2 and mnz2 are not directly intermediate to xnt1 - xnt3 and mnz1 - mnz3, respectively, as would be the case in a simple rising temperature scenario.

It is also noteworthy that at least in our samples the Belcina phosphates were not altered by post-growth processes as are often found in the form of a secondary porosity and/or secondary mineral growth (e.g. [50].

5.2. Phosphate Ages

Mnz1, mnz2, xnt1, and xnt2 show a statistically significant weighted mean CHIME age of 215.9 ± 1.3 Ma (Norian, Upper Triassic). For the further discussion we prefer to use this as geologically relevant. The third-generation phosphate ages are tentatively younger but associated with large analytical uncertainties and thus did not deliver geologically useful age data.

Comment on Pb_{common}: EMP (U+Th)-total Pb ages are often thought of as not providing very reliable age information, as any Pb_{common} contribution cannot easily be detected [30,31,36]. We judge the Pb_{common} contribution in our phosphate analyses to be insignificant. This is based on the argument that all CHIME ages show within analytical uncertainty a regression intercept at Pb (µg/g) = 0 [30,31,51]. Any undetected Pb_{common} would render the ages to be too old. Therefore, the true (Pb_{common} free) ages would be younger and thus the age difference to the intrusives even larger.

5.3. Geological Implications

All published data on the DAM rocks suggest that these have experienced hydrothermal/metasomatic overprinting to strongly various degrees involving different processes and evolutionary stages. Thereby hydrothermal fluids particularly leached REE, HFSE, and actinides from the nepheline syenites of the DAM [5,25]. The fluid source could be a late-stage carbonatite body emplaced below the DAM sensu stricto, as seen in the Spitskop Complex or Kovdor intrusion [5]. Field evidence shows that most likely mafic dykes provided the conduits for the upward migration of these hydrothermal fluids to the roof zone of the DAM. We postulate that the mineralized carbonate veins at Belcina were derived from the same REE- and carbonate-rich hydrothermal fluid source.

The absolute ages for hydrothermal phosphate growth at Belcina (ca. 216 Ma, Middle Norian) show that the three hydrothermal stages followed rapidly after each other, as within the ascribed uncertainties no age trend could be observed for the three phosphates generations. We suggest a duration of less than 1 Ma for the complete vein formation at Belcina. On the other hand, the igneous activities in the DAM took place in the time from ca. 235 Ma (Carnian) to ca. 225 Ma (Lower Norian)

Preprints (www.preprints.org) | NOT PEER-REVIEWED | Posted: 5 May 2023 doi:10.20944/preprints202305.0299.v1

[2]. The obvious age gap of ca. 10 Ma between the latest known igneous phase and the hydrothermal activity in Belcina (and possibly also Jolotca) is too long to support a derivation of the hydrothermal fluids directly from youngest the alkaline DAM melts. The age gap rather supports the above model that the hydrothermal fluids leading to the formation of the mineralized carbonate veins stem from a late-stage intrusion, possibly carbonatitic in composition, but at present not visible at the outcrop level. This is supported by the late stage REE-HFSE-actinides mineralization in combination with the carbonates as such, the significant amounts of Fe oxides/hydroxides and minor sulfides of Fe, Pb, Zn, Mo, and Hg, all these being typical carbonatite features. Also the occurrence of carbonates of different generations as gangue minerals is specific to some mineralizations generated by carbothermal/hydrothermal carbonatite fluids.

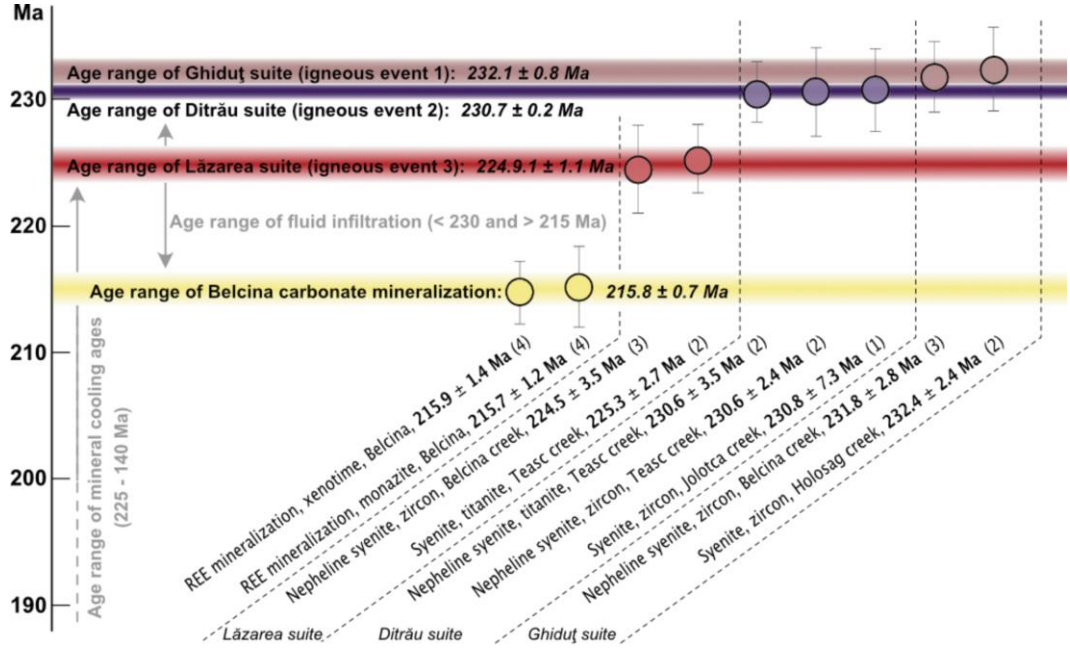

Figure 11. Compilation of the postulated formation age of the Belcina carbonate mineralized veins, the mean intrusion ages for the alkaline rocks of the DAM and the age ranges for metasomatic/hydrothermal overprinting and mineral cooling ages. Data is from (1) - [28]; (2) - [1]; (3) - [2]; (4) - this work.

6. Conclusions

The Belcina REE mineralized carbonate veins situated in the contact aureole of the Ditrău Alkaline Massiv show rock-forming phosphates (monazite-(Ce), xenotime-(Y)), together with apatite, Fe-Mg-rich carbonate, thorite, thorogummite, gedrite and plagioclase. Mineral chemistry, textures and growth ages of monazite-(Ce) and xenotime-(Y) show that the vein formation follows a distinctive three-stage hydrothermal evolution. We propose the presence of at least three distinct mineral paragenesis indicative for the three-stage hydrothermal development of the REE carbonate mineralization:

a) xnt1 + xnt2 + mnz1
b) mnz2 + plagioclase
c) xnt3 + mnz3 + apatite + Fe-dolomite

The relative phosphate age succession (from older to younger) thereby is xnt1 > xnt2 > and/or + mnz1 > mnz2 > mnz3 + xnt3 + apatite. Taking into account the other mineral phases the extended paragenetic succession is xnt1 > xnt2 (>)+ mnz1 + Fe2O3 + Fe-gedrite > mnz2 + Fe-dolomite + plagioclase > mnz3 + xnt3 + apatite. Mineral chemistry shows that the phosphates crystallized from hydrothermal fluids whereby each phosphate type follows an independent evolutionary path suggesting growth from (at least) 3 independent and successive hydrothermal fluids. Chemistry and pathways with the DAM suggest that these hydrothermal fluids could be derived from a (subsurface) carbonatitic intrusion.

Mnz1, mnz2, xnt1, and xnt2 ages are tightly cluster at 215.9 ± 1.3 Ma (Norian, Upper Triassic). The third-generation phosphate ages are tentatively younger but associated with large analytical uncertainties and thus did not deliver geologically useful age data.

The three hydrothermal stages followed rapidly after each other as within the ascribed uncertainties no age trend could be observed for the three phosphates generations. We suggest a duration of less than 1 Ma for the complete vein formation at Belcina. The phosphates were not altered by post-growth processes as for instance no porosity was developed and no secondary minerals are found, i.e., fluid infiltration after the growth of the phosphates did not overprint the existing phosphates, possibly with the exception of the xnt1 generation which partly shows slight resorption effects.

The mean age of ca. 216 Ma is interpreted as timing the carbonate vein formation at Belcina. This, and in line with the fluid chemistry, supports a model of the presence of a late-stage, independent carbonatitic intrusion about 10 Ma after the main igneous activity forming the DAM.

Supplementary Materials: The following supporting information can be downloaded at the website of this paper posted on Preprints.org, Table S1: Monazite-(Ce) EMP data; Table S2: Xenotime-(Y) EMP data.

Author Contributions: All authors have contributed equally to the design of the study. UK and JB conducted the analytical work. All authors contributed equally to data interpretation, presentation and preparation of the manuscript. All authors have read and agreed to the published version of the manuscript.

Funding: The research activities were co-financed by the funds granted under the Research Excellence Initiative of the University of Silesia in Katowice.

Data Availability Statement: The data presented in this study are available in Supplementary Materials, Tables S1 and S2.

Acknowledgments: Gyula Jakab (I.G. Mineral Land, Romania) and Lucian Ionescu (Romanian Waters, S.G.A Harghita, Romania) are thanked for their help in the field and discussions. Franz Biedermann (University of Vienna, Austria) is thanked for the help in sample preparation. Grzegorz Zieliński (Micro-Area Analyses Laboratory, Polish Geological Institute, Warszawa, Poland) helped with the EMP mineral analyses.

Conflicts of Interest: The authors declare no conflict of interest. The funders had no role in the design of the study; in the collection, analyses, or interpretation of data; in the writing of the manuscript; or in the decision to publish the results.

References

1. Pál-Molnár, E.; Kiri, L.; Lukács, R.; Dunkl, I.; Batki, A.; Szemerédi, M.; Almási, E.; Sogrik, E.; Harangi, H. Timing of magmatism of the Ditrău Alkaline Massif, Romania – A review based on new U–Pb and K/Ar data. *Central European Geology* **2021**, 1-20, doi:10.1556/24.2021.00001.
2. Klötzli, U.; Burda, J.; Li, Q.L.; Liu, Y.; Jakab, G.; Ionescu, L.; Tibuleac, P. Petrochronological evidence for a three-stage magmatic evolution of nepheline syenites from the Ditrău Alkaline Massif, Romania. *Minerals* **2022**, 12 (657), 1-27, doi:doi.org/10.3390/min12050657.
3. Hîrtopanu, P.; Andersen, J.C.; Fairhurst, R. Nb, Ta, REE (Y), Ti, Zr, Th, U and Te rare element minerals within the Ditrău alkaline intrusive complex, eastern Carpathians, Romania. Mineralogy of Székelyland, Eastern Transylvania, Romania. *Csik County Nature and Conservation Society*, Miercurea Ciuc. **2010**, 89-128.
4. Hîrtopanu, P.; Andersen, J.C.; Fairhurst, R. Thorite, thorogummite and xenotime-(Y) occurrence in Ditrău alkaline intrusive massif, East Carpathians. *Proceedings of the Romanian Academy of Science, Series B*. **2013,** 15, 111-132.
5. Honour, V.C.; Goodenough, K.M.; Shaw, R.A.; Gabudianu, I.; Hîrtopanu, P. REE mineralisation within the Ditrău Alkaline Complex, Romania: Interplay of magmatic and hydrothermal processes. *Lithos*. 2018;314-315:360-381, doi:10.1016/j.lithos.2018.05.029
6. Jakab, G. Geneza Masivului Alcalin Ditrau. *Editura Mark House*, Gheorgheni **2017**, 1-166.
7. Jakab, G. Geologia Masivului alcalin de la Ditrău. *Editura Mark House*, Gheorgheni **1998**, 1-95.
8. Hîrtopanu, P. New Minerals and Mineral Varieties for Romania. *Vergiliu* **2018**, 1-395.
9. Săbău, G. HFSE and REE vein mineralization associated to the Ditrău Alkaline Massif. *XXXII International Conference on Alkaline Magmatism of the Earth and related strategic metal deposits*, Apatity **2015**, 1-2, doi: http://alkaline.web.ru/2015/Program_en.html.
10. Rudnick, RL.; Gao, S. Composition of the Continental Crust. In: The Crust. Vol 3. *Treaties of Geochemistry*, *Elsevier* **2005**, 1-64.

11. Goodenough, KM.; Schilling, J.; Jonsson, E.; Kalvig, P.; Charles, N., Tuduri, J.; Deady, EA.; Sadeghi, M.; Schiellerup, H.; Müller, A.; Bertrand, G.; Arvanitidis, N.; Eliopoulos, D.G.; Shaw, RA.; Thrane, K.; Keulen, N. Europe's rare earth element resource potential: An overview of REE metallogenetic provinces and their geodynamic setting. *Ore Geology Reviews* **2016**, 72, 838-856, doi:10.1016/j.oregeorev.2015.09.019.
12. Bea, F. Controls on the trace element composition of crustal melts. *Transactions of the Royal Society of Edinburgh-Earth Sciences* **1996**, 87, 33-41.
13. Gratz, R.; Heinrich, W. Monazite-xenotime thermobarometry: Experimental calibration of the miscibility gap in the binary system $CePO_4$-YPO_4. *American Mineralogist* **1997**, 82(7-8), 772-780.
14. Spear, FS.; Pyle JM. Apatite, monazite, and xenotime in metamorphic rocks. In: Kohn MJ, Rakovan J, Hughes JM, eds. *Phosphates: Geochemical, Geobiological, and Materials Importance* **2002**, 48, 293-335.
15. Janots, E.; Engi, M.; Berger, A.; Allaz, J.; Schwarz, JO.; Spandler, C. Prograde metamorphic sequence of REE minerals in pelitic rocks of the Central Alps: implications for allanite-monazite-xenotime phase relations from 250 to 610 degrees C. *Journal of Metamorphic Geology* **2008**, 26(5), 509-526, doi:10.1111/j.1525-1314.2008.00774.x.
16. Berger, A.; Rosenberg, C.; Schaltegger, U. Stability and isotopic dating of monazite and allanite in partially molten rocks: examples from the Central Alps. *Swiss Journal of Geosciences* **2009**, 102(1), 15-29, doi:10.1007/s00015-009-1310-8.
17. Harlov, DE.; Wirth, R.; Hetherington, CJ. Fluid-mediated partial alteration in monazite; the role of coupled dissolution-reprecipitation in element redistribution and mass transfer. *Contributions to Mineralogy and Petrology* **2011**, 162(2), 329-348, doi:10.1007/s00410-010-0599-7.
18. Ondrejka, M.; Putiš, M.; Uher, P.; Schmiedt, I.; Pukančík, L.; Konečný, P. Fluid-driven destabilization of REE-bearing accessory minerals in the granitic orthogneisses of North Veporic basement (Western Carpathians, Slovakia). *Mineralogy and Petrology* **2016**, 110(5), 561-580, doi:10.1007/s00710-016-0432-8.
19. Engi, M. Petrochronology Based on REE-Minerals: Monazite, Allanite, Xenotime, Apatite. *Reviews in Mineralogy and Geochemistry* **2017**, 83(1), 365-418, doi:10.2138/rmg.2017.83.12.
20. Ódri, Á.; Harris, C.; Le Roux P. The role of crustal contamination in the petrogenesis of nepheline syenite to granite magmas in the Ditrău Complex, Romania: evidence from O-, Nd-, Sr- and Pb-isotopes. *Contributions to Mineralogy and Petrology* **2020**, 175(11), 100, doi:10.1007/s00410-020-01738-5.
21. Höck, V.; Ionescu, C.; Balintoni, I.; Koller, F. The Eastern Carpathians "ophiolites" (Romania): Remnants of a Triassic ocean. *Lithos* 2009, 108(1), 151-171, doi:10.1016/j.lithos.2008.08.001.
22. Balintoni, I.; Balica, C.; Ducea, MN.; Hann, HP. Peri-Gondwanan terranes in the Romanian Carpathians: A review of their spatial distribution, origin, provenance, and evolution. *Geoscience Frontiers* **2014**, 5(3), 395-411, doi:10.1016/j.gsf.2013.09.002.
23. Pál-Molnár, E.; Batki, A.; Almási, E.; et al. Origin of mafic and ultramafic cumulates from the Ditrău Alkaline Massif, Romania. *Lithos* **2015**, 239, 1-18, doi:10.1016/j.lithos.2015.09.022.
24. Morogan, V.; Upton, BGJ.; Fitton, JG. The petrology of the Ditrău alkaline complex, Eastern Carpathians. *Mineralogy and Petrology*. **2000**, 69(3), 227-265, doi:10.1007/s007100070023.
25. Fall, A.; Bodnar, R.J.; Szabó, C.; Pál-Molnár, E. Fluid evolution in the nepheline syenites of the Ditrău Alkaline Massif, Transylvania, Romania. *Lithos* **2007**, 95(3), 331-345, doi:10.1016/j.lithos.2006.08.005.
26. Batki, A.; Pál-Molnár, E.; Dobosi, G.; Skelton, A. Petrogenetic significance of ocellar camptonite dykes in the Ditrău Alkaline Massif, Romania. *Lithos* **2014**, 200-201, 181-196, doi:10.1016/j.lithos.2014.04.022.
27. Batki, A.; Pál-Molnár, E.; Jankovics, M.É.; Kerr, A.C.; Kiss, B.; Markl, G.; Heincz, A.; Harangi, S. Insights into the evolution of an alkaline magmatic system: An in situ trace element study of clinopyroxenes from the Ditrău Alkaline Massif, Romania. *Lithos* **2018**, 300-301, 51-71, doi:10.1016/j.lithos.2017.11.029.
28. Pană, D.; Balintoni, I.; Heaman, LM. Precise U-Pb zircon dating of the syenite phase from the Ditrău Alkaline Igneous Complex. *Studia Universitatis Babes-Bolyai, Geologia*. **2000**, 45(1), 79-89.
29. Pyle, JM.; Spear, FS.; Wark, DA. Electron microprobe analysis of REE in apatite, monazite and xenotime: Protocols and pitfalls. In: Kohn MJ, Rakovan J, Hughes JM, eds. *Phosphates: Geochemical, Geobiological, and Materials Importance* **2002**, 48, 337-362.
30. Montel, JM.; Foret, S.; Veschambre, M.; Nicollet, C.; Provost, A. Electron microprobe dating of monazite. *Chemical Geology* **1996**, 131(1-4), 37-53, doi:10.1016/0009-2541(96)00024-1.
31. Cocherie, A.; Albarède, F. An improved U-Th-Pb age calculation for electron microprobe dating of monazite. *Geochimica et Cosmochimica Acta* **2001**, 65(24), 4509-4522, doi:10.1016/S0016-7037(01)00753-0.
32. Suzuki, K.; Adachi, M. Middle Precambrian detrital monazite and zircon from the Hida Gneiss on Oki-Dogo Island, Japan; their origin and implications for the correlation of basement gneiss of Southwest Japan and Korea. *Tectonophysics* **1994**, 235(3), 277-292. http://search.proquest.com/docview/50210704?accountid=14682.
33. Vermeesch, P. IsoplotR: A free and open toolbox for geochronology. *Geoscience Frontiers* **2018**, 9(5), 1479-1493, doi:10.1016/j.gsf.2018.04.001.
34. Dahl, PS.; Hamilton, MA.; Jercinovic, MJ.; et al. Comparative isotopic and chemical geochronometry of monazite, with implications for U-Th-Pb dating by electron microprobe; an example from metamorphic

rocks of the eastern Wyoming Craton (U.S.A.). *American Mineralogist* **2005**, 90(4), 619-638, doi:10.2138/am.2005.1382.
35. Klötzli, U.; Klötzli-Chowanetz, E.; Košler, J. Characterization of a new laser ablation xenotime U-Pb age standard. *Geochimica et Cosmochimica Acta* **2010**, 74, doi:http://search.proquest.com/docview/1017950673?accountid=14682.
36. Konečný, P.; Kusiak, MA.; Dunkley, DJ. Improving U-Th-Pb electron microprobe dating using monazite age references. *Chemical Geology* **2018**, 484, 22-35, doi:10.1016/j.chemgeo.2018.02.014.
37. McDonough, WF.; Sun, S. The composition of the Earth. *Chemical Geology* **1995**, 120(3), 223-253, doi:10.1016/0009-2541(94)00140-4.
38. Repina, SA. Fractionation of REE in the xenotime and florencite paragenetic association from Au-REE mineral occurrences of the Nether-Polar Urals. *Geochemistry International* **2011**, 49(9), 868-887, doi:10.1134/S0016702911090060.
39. Suzuki, K.; Adachi, M.; Kajizuka, I. Electron microprobe observations of Pb diffusion in metamorphosed detrital monazites. *Earth and Planetary Science Letters* **1994**, 128(3-4), 391-405, doi:10.1016/0012-821X(94)90158-9.
40. Harlov, DE.; Förster, HJ. Fluid-induced nucleation of (Y+REE)-phosphate minerals within apatite: Nature and experiment. Part II. Fluorapatite. *American Mineralogist* **2003**, 88(8-9), 1209-1229.
41. Harlov, DE.; Prochazka, V.; Foerster, HJ.; Matejka, D. Origin of monazite-xenotime-zircon-fluorapatite assemblages in the peraluminous Melechov granite massif, Czech Republic. *Mineralogy and Petrology* **2008**, 94(1-2), 9-26, doi:10.1007/s00710-008-0003-8.
42. Alves, FEA.; Neumann, R.; Ávila, CA.; Faulstich, FRL. Monazite-(Ce) and xenotime-(Y) micro-inclusions in fluorapatite of the pegmatites from the Volta Grande mine, Minas Gerais state, southeast Brazil, as witnesses of the dissolution–reprecipitation process. *Mineralogical Magazine* **2019**, 83(4), 595-606, doi:10.1180/mgm.2019.43.
43. Lipin, BR.; McKay, GA. Geochemistry and Mineralogy of Rare Earth Elements, *Reviews in Mineralogy* **1989**, 21, 1-349.
44. Chen W, Liu HY, Lu J, et al. The formation of the ore-bearing dolomite marble from the giant Bayan Obo REE-Nb-Fe deposit, Inner Mongolia: insights from micron-scale geochemical data. *Mineralium Deposita* **2020**, 55(1), 131-146, doi:10.1007/s00126-019-00886-4.
45. Irber, W. The lanthanide tetrad effect and its correlation with K/Rb, Eu/Eu*, Sr/Eu, Y/Ho, and Zr/Hf of evolving peraluminous granite suites. *Geochimica et Cosmochimica Acta* **1999**, 63(3/4), 489-508.
46. Duc-Tin, Q.; Keppler, H. Monazite and xenotime solubility in granitic melts and the origin of the lanthanide tetrad effect. *Contributions to Mineralogy and Petrology* **2015**, 169(8), 1-26, doi:10.1007/s00410-014-1100-9.
47. Anenburg, M.; Williams, MJ. Quantifying the Tetrad Effect, Shape Components, and Ce–Eu–Gd Anomalies in Rare Earth Element Patterns. *Mathematical Geosciences* **2022**, 54(1), 47-70, doi:10.1007/s11004-021-09959-5.
48. Daniel, CG.; Pyle, JM. Monazite-xenotime thermochronometry and Al_2SiO_5 reaction textures in the Picuris range, northern New Mexico, USA: New evidence for a 1450-1400 Ma orogenic event. *Journal of Petrology* **2006**, 47(1), 97-118.
49. Daniel, CG.; Pyle, JM. Integrating monazite and xenotime thermochronology to determine the timing and nature of the Al2SiO5 triple-point metamorphism in the Picuris mountains, New Mexico, USA. *Geochimica Et Cosmochimica Acta* **2010**, 74(12), A206.
50. Tramm, F.; Wirth, R.; Budzyń, B.; Sláma, J.; Schreiber, A. LA-ICP-MS and TEM constraints on the magmatic and post-magmatic processes recorded by the zircon-xenotime intergrowth in pegmatite (Piława Górna, Góry Sowie Block, SW Poland). *Lithos* **2021**, 404-405, 106480, doi:10.1016/j.lithos.2021.106480.
51. Suzuki, K.; Adachi, M.; Kato, T.; Yogo, S. CHIME dating method and its application to the analysis of evolutional history of orogenic belts. *Geochemistry* **1999**, 33(1), 1-22, doi:http://search.proquest.com/docview/51288118?accountid=14682.